

Determination of the Spectral Linewidth Enhancement Factor for Strained InGaAsP Quantum Wire Lasers

A thesis submitted to
the department of Electrical and Electronic Engineering
of
Bangladesh University of Engineering and Technology
in partial fulfillment of the requirements for
the degree of
MASTER OF SCIENCE IN ELECTRICAL AND ELECTRONIC ENGINEERING



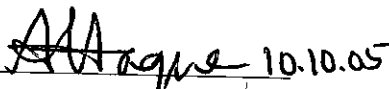


by
Mohammad Abul Khayer

DEPARTMENT OF ELECTRICAL AND ELECTRONIC ENGINEERING
BANGLADESH UNIVERSITY OF ENGINEERING AND TECHNOLOGY
October 2005



The thesis entitled "Determination of the Spectral Linewidth Enhancement Factor for Strained InGaAsP Quantum Wire Lasers" submitted by Mohammad Abul Khayer Roll No.: 040306202P, Session: April, 2003 has been accepted as satisfactory in partial fulfillment of the requirements for the degree of MASTER OF SCIENCE IN ELECTRICAL AND ELECTRONIC ENGINEERING.

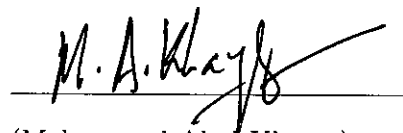
BOARD OF EXAMINERS

1.  10.10.05 Chairman
(Dr. Anisul Haque)
Professor
Department of Electrical and
Electronic Engineering, BUET,
Dhaka-1000, Bangladesh
2.  Member
(Ex-officio)
(Dr. S. Shahnawaz Ahmed)
Professor and Head
Department of Electrical and
Electronic Engineering, BUET,
Dhaka-1000, Bangladesh
3.  Member
(Dr. Md. Quamrul Huda)
Associate Professor
Department of Electrical and
Electronic Engineering, BUET,
Dhaka-1000, Bangladesh
4. A. Hossain. Member
(External)
(Dr. A. K. M. Akther Hossain)
Associate Professor
Department of Physics, BUET
Dhaka-1000, Bangladesh

Declaration

It is hereby declared that this thesis or any part of it has not been submitted elsewhere for the award of any degree or diploma.

Signature of the candidate



(Mohammad Abu Khayer)

Acknowledgements

I wish to convey my heartiest gratitude and profound respect to my supervisor Dr. Anisul Haque, Professor, Department of Electrical and Electronic Engineering (EEE), Bangladesh University of Engineering and Technology (BUET), Bangladesh, for his continuous guidance, constructive suggestions and whole-hearted supervision throughout the progress of this work, without which this thesis could never be materialized. I am deeply grateful to him for his continuous efforts to make me acquainted with the world of advanced research.

I am grateful to the Head, Dept. of EEE, Bangladesh University of Engineering and Technology (BUET), who provided with all the facilities of Simulation laboratory of the department. I like to express my deep gratitude to Dr. Mohammad Ali Choudhury, Professor, Dept. of EEE, BUET for his continuous encouragement. I also like to express thanks and gratitude to Dr. M. M. Shahidul Hassan, Professor, Dept. of EEE, BUET for his encouragement. I want to thank A. N. M. Zainuddin, Lecturer, Dept. of EEE, Ahmad Ehteshamul Islam, Lecturer, Dept. of EEE, BUET for their continuous encouragement and valuable discussions.

And I am deeply indebted to my mother, my brothers, my sister and my wife for their encouragement, patience and love.

Dedication

To My Father.
(May his soul rest in eternal peace.)

Contents

Acknowledgements	iii
Dedication	iv
List of Tables	vii
List of Figures	viii
Abstract	xi
1 Introduction	1
1.1 Literature Review	4
1.2 Objective of the Work	7
1.3 Organization of the Thesis	8
2 Theory	9
2.1 Multiband Hamiltonian	9
2.2 Strain Analysis	12
2.2.1 Strain in Semiconductor Devices	12
2.2.2 Strain Effects on Electronic States	13
2.3 Electron-Photon Interactions	14
2.4 Gain Spectrum	15
2.5 Linewidth Enhancement Factor	16
3 Calculation Procedure	18
3.1 Device structure	18
3.2 Material Properties of InGaAsP Systems	18
3.3 Analytical Expressions for Strain Distribution	20
3.4 Calculation of Electronic States	23

3.5	Calculation of Transition Matrix Elements	27
3.6	Calculation of Reduced Density of States and Quasi-Fermi Energies	28
3.7	Calculation of Gain Spectrum	29
3.8	Calculation of Linewidth Enhancement Factor	31
4	Results and Discussions	33
4.1	Dispersion relationships for QWires	33
4.2	Gain Characteristics	34
4.3	Refractive Index Change	42
4.4	Linewidth Enhancement Factor	42
4.4.1	Variation of Barrier Strain	45
4.4.2	Variation of number of QWire layers in the active region .	45
4.4.3	Variation of Wire width	49
5	Conclusions	54
5.1	Summary	54
5.2	Suggestions for Future Works	55
	Bibliography	57

List of Tables

3.1	Material Constants	20
4.1	Comparison of key dispersion relationship parameters for 10-, 20-, and 30-nm wide QWires as shown in Figs. 4.1 and 4.2	34
4.2	Wave guide loss of single-layer QWires and QWell for 0.15% TS barriers with mode occupation factor, Γ_{act} of 1%/well.	47
4.3	Lasing wavelength, threshold carrier density and α -factor for different QWires and QWell structure with 0.15% TS barriers and with single-layer stack.	51

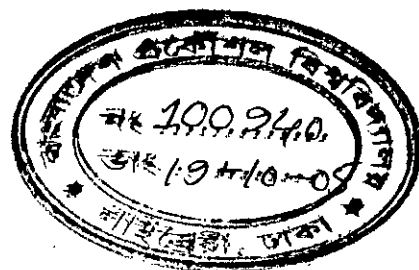
List of Figures

3.1	Cross-sectional schematic diagram of a vertical stack of multiple QWire structures.	19
3.2	Lattice parameter vs bandgap energy for the binary and ternary material system.	21
3.3	Cross-sectional schematic diagram of a buried strained layer. Important dimension and the coordinate axes are indicated.	22
4.1	Dispersion relationships for the two lowest conduction and the three highest hole subbands in (a-c) 10-nm and (d-f) 20-nm wide QWires calculated for three different types of barriers.	35
4.2	Dispersion relationships for the three highest hole subbands in (a-c) 30-nm and (d-f) 50-nm wide QWires calculated for three different types of barriers.	36
4.3	Transition matrix elements M_{11} as functions of wave vector k in a 20-nm-wide QWire for three types of barriers (a) and for different number of QWire layers in the active region with 0.15% TS barriers (b). Only $TE_{ }$ polarization are considered.	38
4.4	Material gain as a function of photon energy in a 20-nm-wide single-layer QWire (a-c), 30-nm-wide single-layer QWire (d-f) for LM and two types of TS barriers.	39
4.5	Peak material gain G at lasing frequency as a function of carrier density n in a 10-nm-wide QWire (a), 20-nm-wide QWire (b), 30-nm-wide QWire (c) and 50-nm-wide QWire (d) for LM and two TS barriers. QWires of single-layer structure are considered.	40
4.6	Peak material gain G as a function of carrier density n in a single-layer QWire structure with LM and two types of TS barriers for different wire widths (a)-(c).	41

4.7	Peak material gain G as a function of carrier density n in 10-nm (a), 20-nm (b) and 50-nm (c) wide QWires with 0.15% TS barriers for different number of QWire layers in the active region.	43
4.8	Both real part (a)-(b) and imaginary part (c)-(d) of refractive index change as a function of the injected carrier density at gain peak energy of single-layer QWire structures for wire widths of 10-nm and 20-nm, respectively.	44
4.9	α -factor as a function of photon energy for single-layer QWire structure with wire widths of 20-nm (a), and 50-nm (b). The arrows point at the photon energy at which lasing would occur. . .	46
4.10	α -factor as a function of the injected carrier density at gain peak position of single-layer QWire structure with LM and two types of TS barriers for wire widths of (a) 10-nm, (b) 20-nm, (c) 30-nm and (d) 50-nm.	48
4.11	α -factor as a function of the injected carrier density at gain peak position of QWire structures with different number of QWire layers with 0.15% TS barriers for wire widths of (a) 10-nm, (b) 20-nm, (c) 30-nm and (d) 50-nm.	49
4.12	α -factor as a function of the injected carrier density at gain peak position of single-layer QWire structures with different wire widths for (a) LM (b) 0.15% TS and (c) 0.60% TS barriers.	50
4.13	Material gain as a function of the photon energy (a) and peak material gain as a function of the injected carrier density (b) for a QWell laser with 0.15% TS barriers.	52
4.14	α -factor as a function of the injected carrier density for different wire widths with LM and two types of TS barriers. α -factor for QWell structure is also presented for comparison.	53

Abstract

Linewidth Enhancement Factor, also termed as α -factor, of compressively strained (CS) InGaAsP/InP quantum wire (QWire) lasers is theoretically investigated and fundamental trend in the behavior of α -factor is studied. The structure consists of single or multiple layers of InGaAsP CS QWires and tensile-strained (TS) or lattice-matched (LM) barriers grown on (001) InP substrate. The band structures of the CS InGaAsP QWires are calculated using an 8 band $\mathbf{k} \cdot \mathbf{p}$ model including elastic strain relaxation effects. Changes in the imaginary part of the refractive index is easily found from the gain spectra and changes in the real part is evaluated from the changes in imaginary part through Kramers-Kronig transformation. Dependence of α -factor, which relates the real and imaginary parts of refractive index due to a change in the injected carrier density, on device parameters such as wire width, barrier strain and number of vertically stacked QWire layers, are evaluated. It is found that α -factor decreases significantly with decreasing wire width and exhibits less dependence on carrier density. Also, α -factor is the highest when the barriers are LM to the InP substrate and is drastically reduced when the TS in the barriers is increased in a strain compensating (SC) scheme. Moreover, QWire structures with multiple-layer exhibits lower value of α -factor compared to the one with single-layer structure. It is found that improvements in the α -factor relative to quantum well (QWell) laser for 0.15% TS barriers, is not achieved unless wire width is reduced below 30 nm. However, among all the structures, the maximum value of the α -factor is the highest for the QWell and this maxima monotonically decreases with decreasing wire width.



Chapter 1

Introduction

Remarkable advances in semiconductor technology have made possible the fabrication of artificial nanostructures with dimensions comparable to inter-atomic distances. The availability of this class of semiconductor structures creates new avenues for the investigation of the physics of condensed matter under conditions of greatly reduced dimensionality where 'quantum size effect' become apparent. In the case of electrons, quantum size effects occur when the physical dimensions are comparable to the characteristic lengths that determine electron behavior. The great current interest in semiconductor nanostructure research is stimulated by a continuous stream of discoveries and the potential to revolutionize the technology of solid state optoelectronics. By growth with molecular beam epitaxy (MBE) technique and, more recently, by metal-organic-chemical-vapor deposition (MOCVD) technique, it is possible to obtain ultra-thin semiconductor layers that are smooth on an atomic scale. New physics and novel devices are possible because of the excellent control of material compositions and doping. Single heterojunctions and multiple heterostructures based on two different semiconductors are now routinely grown in many laboratories. Semiconductor lasers are one of the most successful photonic devices benefited by quantum-size effects, since their operational characteristics have been drastically improved by the introduction of quantum well (QWell) structures [1]. Recent efforts have concentrated on reducing the dimensionality further to quantum wire (QWire) [2] and quantum dot (QDot) [3] devices in which the carriers are restricted to one or zero dimensions, respectively. Increased confinement of carriers means that QWire and QDot semiconductor lasers are expected to possess improved performances, such as, lower threshold current, higher differential gain and narrower linewidth,

compared to their QWell and bulk counterparts.

In the III-V semiconductors, the material system commonly used to fabricate semiconductor lasers, there is a serious asymmetry between the very light conduction band mass and the heavy valence band mass. Ideally both masses should be as light as possible. The density of states would then be very small and the carrier density required for transparency would be minimized. Introduction of strain in the active region of semiconductor lasers reduces the asymmetry of electron and hole effective masses [4], [5] and this concept has successfully been applied to multi-quantum-well structures [6]. It is shown [7] that the growth of strained QWell structures, where the QWell is under bi-axial compression, leads to improved performance in III-V semiconductor lasers. These improvements were predicted because the built-in axial strain in the QWell layer splits the degeneracy of the light-hole (LH) and heavy-hole (HH) states at the valence band maximum, and can lead to the highest valence subband having a low effective mass in the QWell plane. This reduces the number of carriers required to achieve population inversion and hence may lead to a reduced current density and increased differential gain at threshold [8]. It is also suggested that the reduced valence band mass may lead to the virtual elimination of the intrinsic loss mechanisms of intervalence band absorption (IVBA) and Auger recombination [5] which, in some cases, contribute to the nonequilibrium population of the split-off valence band [9]. The crystalline structure of essentially all important semiconductors consists of an FCC lattice with a two atom basis. This results in a diamond or zinc blend crystal structure and has important consequences for the bandstructure of the semiconductors. For the direct bandgap materials, the conduction band minimum state has an s-type symmetry with a small p-type admixture away from the zone edge. Due to the s-type nature of the conduction band edge, strain mainly shifts the edge with only a small change in the conduction band curvature [10]. The valence band edge states of all semiconductors are essentially similar. At the zone centre, one has a doubly degenerate state corresponding to the HH and LH bands while the split-off (SO) state is present at an energy given by the spin-orbit coupling. The character of the HH, LH and SO states is given in the total angular momentum basis $|j, m\rangle$ by $|\frac{3}{2}, \pm\frac{3}{2}\rangle$, $|\frac{3}{2}, \pm\frac{1}{2}\rangle$ and $|\frac{1}{2}, \pm\frac{1}{2}\rangle$, states, respectively.

The angular dependence of these states is given by the p-type functions. In order to study the effect of strain on electronic properties of semiconductors, it is first essential to establish the strain tensor produced by epitaxy. Once the strain tensor is known, one can apply the deformation potential theory [11] to calculate the effects of strain on various eigenstates in the Brillouin zone.

As mentioned earlier, recent progress in epitaxial growth and processing techniques is making it possible to realize quaternary QWire structures where carriers are confined two-dimensionally. They attract much interest due to their novel physical properties and consequent improvements of device performance. By using QWires, higher gain and lower threshold current is expected [12]. Consideration of strain effects on band structures is important in these kinds of structures when the wires are buried in larger band gap materials with different lattice constants. These are referred to as strained wires. In strained wires, strain can also exist in the surrounding matrices as well as in the wires, so it is not straightforward to obtain strain components from lattice mismatch. Moreover, like improvements that can be achieved by adopting strained QWells in laser diodes [4], [7], [10], [13]-[19], characteristic improvements may also be expected in strained QWires when the valence band structure is modified by anisotropic strain [12]. Accordingly, it is important to study the strain effect in wires. In contrast, the presence of strain may lead to structural problems resulting in accelerated degradation of the device [20]. Strain relaxation in laser structures, whereby material reverts wholly or partially to its preferred lattice spacing, may lead to modifications of the electronic band structures, possibly resulting in photon absorption [21] or to enhanced migration of certain atoms to or from relaxed regions of the crystal [22]. Both effects could possibly lead to faster degradation of the laser. In many practical laser structures, the active region consists of a series of strained layers forming a MQWell stack buried below the surface so that the effect of free surfaces on strain distributions is negligible to a good approximation [20], [22].

The strained QWire is, thus, one of the greatest successes in recent semiconductor band structure engineering technology. The semiconductor band structure can be controlled by making use of quantum confinement and strain, both

of which can be effectively varied by artificial parameters such as well size and composition. Strain-compensated (SC) MQWire lasers have successfully been realized practically with a fabrication method which combines electron beam lithography (EBL), CH_4/H_2 reactive ion etching (RIE) and organometallic vapor-phase-epitaxial (OMVPE) regrowth [23]. This method is very attractive for In-GaAsP/InP lasers consisting of low dimensional systems, such as QWire and QDot structures. Low-damage properties of the etched/regrown interface of In-GaAsP/InP fine structure with a SC MQWell initial wafer was experimentally confirmed [23].

Spectral linewidth enhancement factor, also called α -factor, is an important parameter to characterize the dynamic performance of semiconductor lasers. Narrow spectral linewidth in semiconductor laser is desired for increasing the transmission capacity in optical communication systems, as well as for resolving accuracy in optical measurement system [24]. It may also be an important device parameter in future applications of injection lasers that utilize the coherence of the laser light, such as heterodyne detection of optical signals [25]. The spectral linewidth of the laser, which is enhanced due to the variation of the real refractive index n' with carrier density, can be thought of due to fluctuations in the phase of the optical field and these fluctuations arise from the spontaneous emission events, which discontinuously alter the phase and intensity of the lasing field [25]-[26]. The spectral broadening is explained [27] noting that the refractive index in the active region is a weak function of the carrier concentration, with the index increasing with decreasing carrier density [28]-[30]. Thus during the emission of the pulse, the carrier density decreases causing an increase in the index and a shift of the emission to longer wavelength [27].

1.1 Literature Review

A narrow spectral linewidth in semiconductor lasers is desirable in order to meet the requirements for ultra-fast communication systems using the optical fibre. A great deal of work on the spectral linewidth in injection lasers has been reported [24]-[27]. While significant efforts have been made to understand the effects of spectral dependence on change of carrier density and to improve the α -factor for

QWell lasers, very little work has been done for the QWire structures. In this section, partial reviews of the works done on spectral linewidth are presented.

The α -factor couples the imaginary and real part of refractive index [25] and the refractive index in the active layers of semiconductor laser is again carrier density dependent [31]. Henry *et al.* [32] determined the index change due to the cause of changes in absorption edge of GaAs lasers. They converted the spontaneous emission spectrum to a gain spectrum from which changes in the imaginary part of the refractive index was calculated. The real change in the refractive index was calculated through Kramers-Kronig transformation.

Henry *et al.* [25] first derived the detail theory for laser linewidth. His explanation of the linewidth broadening in semiconductor lasers was based on the observation that each spontaneous emission event not only brings an instantaneous change of optical intensity and phase, but also an additional phase shift caused by the refractive index dependence on carrier density. The coupling of phase and intensity leads then to occurrence of α in the phase rate equation and the laser linewidth is broadened by a factor of $(1 + \alpha^2)$.

Arakawa *et al.* [33] investigated theoretically the α -factor for both single- and multiple-quantum well AlGaAs lasers showing the effects of the number and the thickness of the QWell on the α -factor. Their results indicate that the laser linewidth is significantly suppressed, by $\sim 1/10$, in a SQWell laser compared to a conventional double heterostructure (DH) laser, although they did not include strain in the structure. A possibility of α , the LEF, being reduced to zero and even reaching a negative value has also been raised by them. This behavior of QWell structures is due to a peak of differential gain at photon energies of 150 meV above the bulk bandgap. However the photon energies corresponding to the maximum gain are in the range of 40-50 meV above the bandgap. Hence the photon energies at which α becomes zero are much larger than the lasing photon energy, and in practice the value of α will stay positive. It was reported by Osiński *et al.* [34] that, on average, the values of α are larger for InGaAsP/InP than for AlGaAs DH lasers, with more reliable estimates of α ranging from 4.5

to 7.

Mullane *et al.* [35] theretically investigated the means to minimize the α -factor in tensile-strained QWell lasers using a detailed microscopic model including many-body effects, strain, and valence subband mixing. They analyzed the effects of well width and strain on the α -factor. They observed that the α -factor in highly tensile-strained devices displays reduced sensitivity to the device threshold gain. It also offers improved performance at wider well widths contrasting to unstrained and compressively strained structures.

Willatzen *et al.* [36] calculated the α -factor, for QWires and QDots including the valence band mixing effects. They showed that the α -parameter is smaller than 1 for the sub-two-dimensional structures and concluded that the inclusion of HH-LH mixing in the valence band is extremely important for the QDot and QWire problems.

Seo *et al.* [37] presented a theoretical analysis of the many body effects on the α -factor of the InGaAs/InP strained QWire lasers based on the semiconductor Bloch equations. They showed the α -factor increases with increasing carrier density in free-carrier model but decreases or remain nearly constant in the microscopic model. The spin-orbit coupling effect on the α -factor of the system was also investigated using the 6×6 Luttinger-Kohn Hamiltonian [38].

Oksanen *et al.* [39] calculated the α -factor for QDot and QWell structures in the quasi-equilibrium distribution and parabolic band approximations and showed that QDot offers lower value of α -factor compared to the QWell. They found that the dominant contribution to the α -factor results from the QDot ground state emission line itself.

Schneider *et al.* [40] reported the measurements of the α -factor in an electrically pumped InGaAs QDot amplifier in the temperature range from 50K to room temperature. They observed the α -factor to increase with increasing carrier density and to decrease with increasing photon energy at all investigated temper-

atures.

Many studies have so far been done relating the α -factor for semiconductor lasers using QWell structures. It is generally believed that the value of α is smaller in MQWell laser than in bulk laser and it is even further reduced in lower dimensional systems, QWires and QDots. However, not enough investigations have been done on α -factor of QWires to determine its trend and behavior with respect to the variations in the material and device parameters.

1.2 Objective of the Work

When the level of excitation of a semiconductor laser is raised from zero bias up to threshold, the absorption at the laser line changes to gain with a peak value just large enough to overcome the waveguide losses and at the same time real and imaginary parts of the refractive index are also changed which alters the α -factor. At the laser line, which is at the low energy side of the maximum index changes, the changes in both the real and imaginary parts of the index have the same sign, they are both negative. The change in the real index has a defocusing effect, which must be taken into account in any detailed theory of gain guided lasers [32]. The gross broadening of the spectral lines of pulsating lasers has been attributed to the change in refractive index with carrier density [41]. Thus, spectral α -factor is an important parameter to characterize the dynamic performance of semiconductor lasers.

In this research, the α -factor of InGaAsP/InP compressively strained (CS) QWire lasers is calculated. The α -factor of strained QWell lasers is also calculated and compared to that of QWire lasers to identify the improvement in dynamic performance caused by the additional carrier-confinement in QWires. Effects of non-parabolicity due to material properties, quantum-confinement and elastic strain relaxation are incorporated in the calculation. Finally, we investigate the effects of variation of device parameters, such as, QWire width, strain, multi-well stack, etc. on the α -factor which allows optimizing device design to minimize the α -factor.

1.3 Organization of the Thesis

Chapter 2 discusses the basic theory behind this work. In this chapter, theories to model the strained QWire and QWell quaternary lasers are presented. Chapter 3 describes the calculation procedure. Chapter 4 deals with the calculated results and discussions. In this chapter, various results obtained regarding the α -factor of the QWire and QWell lasers are reported and the comparison made to identify the improvements in dynamic performance of QWire lasers due to the additional carrier-confinement over QWell lasers. Also, at last, the effects of variation of device parameters on the α -factor are discussed. Concluding remarks of this work along with suggestions for future work are presented in chapter 5.

Chapter 2

Theory

In this chapter, the basic theories behind modeling the QWire and QWell quaternary lasers are presented. Finally, the calculation method of spectral α -factor is discussed.

2.1 Multiband Hamiltonian

The multiband effective mass equation [42] is widely used to describe the bandstructures of QWells, QWires and QDots. It can be expressed as,

$$i\hbar \frac{\partial}{\partial t} \Psi_\nu(\mathbf{r}, t) = \sum_{\nu'} H_{\nu\nu'}(-i\nabla) \Psi_{\nu'}(\mathbf{r}, t) + U(\mathbf{r}, t) \Psi_\nu(\mathbf{r}, t), \quad (2.1)$$

where ν represents band index and $H_{\nu\nu'}(\mathbf{k})$ is defined as

$$H_{\nu\nu'}(\mathbf{k}) = \begin{cases} \frac{\hbar^2 k^2}{2m_0} + E_{\nu 0}, & \nu' = \nu \\ \frac{\hbar \mathbf{P}_{\nu\nu'} \cdot \mathbf{k}}{m_0}, & \nu' \neq \nu. \end{cases} \quad (2.2)$$

$P_{\nu\nu'}$ is called the momentum matrix element between bands ν and ν' and is defined as

$$P_{\nu\nu'} = -i\hbar \langle \bar{u}_{\nu,0} | \nabla \bar{u}_{\nu',0} \rangle. \quad (2.3)$$

Here $u_{\nu,0}$ represents the zone center Bloch functions for the ν th band. The relation between the actual wavefunction and the multiband envelope functions follows readily from,

$$\Psi_0(\mathbf{r}, t) = \sum_{\nu} u_{\nu,0}(\mathbf{r}, t) \Psi_\nu(\mathbf{r}, t). \quad (2.4)$$

Eq. (2.1) can be solved for the perfect spatially uniform semiconductor using a variety of well known techniques, but in a QWell or QWire the crystal composition and/or strain varies from region to region and approximations are needed in

order to solve Eq. (2.1). Many such approximate methods are now well known and are extensively used [43]. In our work, we apply an 8-band $\mathbf{k} \cdot \mathbf{p}$ method [44]. The choice of how many bands will be needed depends on the details of the problem to be solved. For our work, we included eight basis functions in the set, namely, the spin-up and spin-down s and p atomic orbital-like states. These are arranged in the following order: $|S \uparrow\rangle$, $|X \uparrow\rangle$, $|Y \uparrow\rangle$, $|Z \uparrow\rangle$, $|S \downarrow\rangle$, $|X \downarrow\rangle$, $|Y \downarrow\rangle$ and $|Z \downarrow\rangle$. As a result, the multiband effective mass equation is transformed into eight coupled differential equations.

In the basis of the eight zone-centre Bloch functions described above, the matrix H takes the form:

$$H = \begin{bmatrix} G & \Gamma \\ -\Gamma^* & G^* \end{bmatrix}, \quad (2.5)$$

where G and Γ are both 4×4 matrices.

The matrices $G(\mathbf{k})$ and Γ are defined as follows [44]:

$$G(\mathbf{k}) = G_1(\mathbf{k}) + G_2(\mathbf{k}) + G_{so}, \quad (2.6)$$

where

$$G_1 = \begin{bmatrix} E_c & iPk_x & iPk_y & iPk_z \\ -iPk_x & E_{v'} & 0 & 0 \\ -iPk_y & 0 & E_{v'} & 0 \\ -iPk_z & 0 & 0 & E_{v'} \end{bmatrix}, \quad (2.7)$$

$$G_2 = \begin{bmatrix} A'k^2 & Bk_yk_z & Bk_xk_z & Bk_xk_y \\ Bk_yk_z & L'k_x^2 + M(k_y^2 + k_z^2) & N'k_xk_y & N'k_xk_z \\ Bk_zk_x & N'k_xk_y & L'k_y^2 + M(k_x^2 + k_z^2) & N'k_yk_z \\ Bk_xk_y & N'k_xk_z & N'k_yk_z & L'k_z^2 + M(k_x^2 + k_y^2) \end{bmatrix}, \quad (2.8)$$

and

$$G_{so} = -\frac{\Delta}{3} \begin{bmatrix} 0 & 0 & 0 & 0 \\ 0 & 0 & i & 0 \\ 0 & -i & 0 & 0 \\ 0 & 0 & 0 & 0 \end{bmatrix}. \quad (2.9)$$

The matrix Γ is:

$$\Gamma = -\frac{\Delta}{3} \begin{bmatrix} 0 & 0 & 0 & 0 \\ 0 & 0 & 0 & -1 \\ 0 & 0 & 0 & i \\ 0 & 1 & -i & 0 \end{bmatrix}. \quad (2.10)$$

All the parameters appearing in Eqs. (2.7)-(2.10) are real. The parameters A' , B , L' , M and N' are known as Kane parameters and are defined in [44]. The parameter B , which is equal to zero for crystals with inversion symmetry, is set to zero in our calculation as well. The parameter P , which is known as the optical matrix element, is proportional to the momentum matrix element between the conduction band and the valence band:

$$P = -i \frac{\hbar}{m_0} \langle S | p_i | i \rangle, \quad (2.11)$$

where $i = X, Y \text{ or } Z$. The parameter P plays an important role in calculating the optical transition strength. The quantity Δ is the spin orbit splitting parameter, while E_c and E_v are the band edge energies in the absence of the spin-orbit coupling.

For bulk structures, each component of \mathbf{k} in Eq. (2.5) is a number, but for low dimensional structures, k_n along each confined direction n is replaced by the differential operator $-i\delta/\delta x_n$. Considering the components of the \mathbf{k} vector in Eq. (2.5) to be numbers and diagonalizing the matrix for a bulk crystal for $k = 0$, one can obtain the dispersion relationships, namely, the \mathbf{k} dependent eigenvalues $E_n(\mathbf{k})$.

For a bulk crystal for $k = 0$, solving the dispersion relation to second order in \mathbf{k} allows one to obtain:

$$\begin{aligned} \frac{m_0}{m_{hh}(100)} &= \gamma_1 - 2\gamma_2, & \frac{m_0}{m_{lh}(100)} &= \gamma_1 + 2\gamma_2 \\ \frac{m_0}{m_{hh}(111)} &= \gamma_1 - 2\gamma_3, & \frac{m_0}{m_{lh}(111)} &= \gamma_1 + 2\gamma_3 \\ \frac{m_0}{m_e} &= \frac{2m_0}{\hbar^2} \left(A' + \frac{P^2(E_g + \frac{2}{3}\Delta)}{E_g(E_g + \Delta)} \right) \\ \frac{m_0}{m_{so}} &= \gamma_1 - \frac{2m_0 P^2 \Delta}{3\hbar^2 E_g(E_g + \Delta)}, \end{aligned} \quad (2.12)$$

where $m_{hh(lh)}(ijk)$ is the heavy (light) hole band edge effective mass in the (ijk) crystallographic direction, m_e is the conduction band effective mass and m_{so} is the split-off band effective mass. The γ_i are known as the Luttinger parameters [44]. In terms of the γ_i , the constants in the matrix are given by:

$$\begin{aligned} L' &= -\frac{\hbar^2}{2m_0}(1 + \gamma_1 + 4\gamma_2) + \frac{P^2}{E_g} \\ M &= -\frac{\hbar^2}{2m_0}(1 + \gamma_1 - 2\gamma_2) \\ N' &= -\frac{3\hbar^2}{m_0}\gamma_3 + \frac{P^2}{E_g}, \end{aligned} \quad (2.13)$$

where $E_g = E_c - E_v$ is the band gap with $E_v = E_{v'} + \frac{\Delta}{3}$. The mathematical relations described in Eqs. (2.13)-(2.14) define all the 8×8 Hamiltonian parameters in terms of the experimental bandgap, effective masses and the spin-orbit splitting.

2.2 Strain Analysis

Strained layer buried heterostructure lasers are becoming increasingly important for optoelectronic applications, for example, in optical communication systems. The strain is predicted to reduce loss mechanisms [4] and strained-layer lasers are therefore expected to exhibit improved performances over their lattice-matched (LM) counterparts. Structural problems associated with strain have motivated the theoretical calculation of strain distribution in a variety of structures [20].

2.2.1 Strain in Semiconductor Devices

A crystal lattice which feels an external force will react by distorting in some fashion. The strained state of the lattice is usually defined by a strain tensor. The introduction of compressive strain (CS) into the crystal lattice of a semiconductor could lead to enhanced performance in semiconductor lasers. Strain can play an important role in both QWell and QWire devices, whether that strain has been deliberately introduced to enhance the properties of the devices or whether strain is present as an unavoidable consequence of the use of different materials. The influence of a uniform strain field in QWell devices is by now well understood but, because of the reduced symmetry, the strain field in QWire structure is

nonuniform and can have a strong influence on the wire's electronic properties. Moreover, the strain field in QWire structures extends into the matrix material, providing additional complications. It is natural, therefore, to expect that strain will prove an important factor in QWire devices and indeed a large proportion of the QWire structures grown to date have employed lattice-mismatched materials.

2.2.2 Strain Effects on Electronic States

Most of the theoretical work assumes that materials are continuous, linear, isotropic and obeys Hooke's Laws. Semiconductor materials are anisotropic but calculations have shown that anisotropy only modifies strain distributions by a small amount [21].

The $\mathbf{k} \cdot \mathbf{p}$ 8×8 bulk Hamiltonian described by Eqs. (2.9)-(2.14) acquires extra terms when the crystal is strained. The strain interaction couples only parallel spins and hence this interaction adds an additional term G_{strain} to original Hamiltonian matrix H in Eq. (2.5). The additional matrix is:

$$G_{strain} = \begin{bmatrix} a_c[e_{xx} + e_{yy} + e_{zz}] & b'e_{yz} - iP \sum_j e_{xj} k_j & b'e_{zx} - iP \sum_j e_{yj} k_j & b'e_{xy} - iP \sum_j e_{zj} k_j \\ b'e_{yz} + iP \sum_j e_{xj} k_j & le_{xx} + m(e_{yy} + e_{zz}) & ne_{xy} & ne_{xz} \\ b'e_{zx} + iP \sum_j e_{yj} k_j & ne_{xy} & le_{yy} + m(e_{xx} + e_{zz}) & ne_{yz} \\ b'e_{xy} + iP \sum_j e_{zj} k_j & ne_{xz} & ne_{yz} & le_{zz} + m(e_{xx} + e_{yy}) \end{bmatrix}, \quad (2.14)$$

where e_{ij} are the strain tensor components. The constants l , m and n are related to the material deformation potentials by:

$$\begin{aligned} a_v &= \frac{1}{3}(l + 2m), \\ b_v &= \frac{1}{3}(l - m), \end{aligned} \quad (2.15)$$

and

$$d_v = \frac{1}{\sqrt{3}}n$$

where a_c is the conduction band hydrostatic deformation potential, a_v is the valence band hydrostatic deformation potential, b_v is the valence band shear deformation potential associated with strain along the [001] crystallographic direction and d_v is the shear deformation potential for strain along the [111] direction.

2.3 Electron-Photon Interactions

Optical gain in semiconductors is caused by photon-induced transitions of electrons from the conduction band to the valence band. Thus in order to understand optical gain, we need to characterize electron-photon interactions in the crystal. To examine the interaction, we represent the photon classically by an electromagnetic wave. The wave's interaction with the electron enters into the Schrödinger equation through the vector potential \mathbf{A} . This interaction with radiation is found by replacing \mathbf{p} in the single electron Hamiltonian by,

$$\mathbf{p}^2 \rightarrow (\mathbf{p} + e\mathbf{A})^2 \approx \mathbf{p}^2 + 2e\mathbf{A} \cdot \mathbf{p}, \quad (2.16)$$

where e is the magnitude of the electron charge. In expanding the square, we have neglected the squared vector potential term, since it does not affect our final results (orthogonality of the wavefunctions ensures that the operator \mathbf{A}^2 does not perturb the system, assuming we can neglect the spatial variation of \mathbf{A} within one unit cell). Substituting Eq. (2.16) into the single electron Schrödinger equation, we can write the new Hamiltonian as

$$H = H_0 + [H_{rad}(\mathbf{r})e^{-i\omega t} + h.c.], \quad (2.17)$$

where $h.c.$ stands for the Hermitian conjugate and it simply means that we take the complex conjugate of all terms except the Hermitian operator \mathbf{p} . The terms in brackets can be viewed as a time-dependent perturbation to the original Hamiltonian H_0 . The effect of this perturbation is to induce electronic transitions between conduction and valence bands. The perturbation Hamiltonian H_{rad} is given by,

$$H_{rad} = \frac{e}{m_0} \mathbf{A} \cdot \mathbf{p} = \frac{e}{2m_0} \mathbf{A}_0 \cdot \mathbf{p} (e^{i\omega t} + e^{-i\omega t}). \quad (2.18)$$

The term $e^{i\omega t}$ induces upward transitions while the term $e^{-i\omega t}$ induces downward transitions. In quantifying the gain, we need to know the number of transitions

that will occur per second in the crystal in response to a given photon flux in a given optical mode. This is accomplished by studying the time evolution of a given electron wavefunction Ψ , initially in the conduction band state, ψ_e , as it makes a transition to the valence band. Inserting the wavefunction into the time-dependent single electron Schrödinger equation, it is possible to obtain an approximate expression for the probability of finding the electron in a particular state in the valence band as a function of increasing time. The time derivative of this time-dependent probability then gives an approximate expression for the transition rate from the conduction band state ψ_e , to a particular valence band state ψ_h . Thus, both the upward and downward rates can be calculated using Fermi's golden rule [45],

$$W_{e \rightarrow h} = \frac{2\pi}{\hbar} |H_{rad(eh)}|^2 \delta(E_e - E_h - \hbar\omega). \quad (2.19)$$

Here, $H_{rad(eh)}$ is given by

$$|H_{rad(eh)}|^2 = \left(\frac{eA_0}{2m_0} \right)^2 |M_{cv}|^2, \quad (2.20)$$

where M_{cv} is the transition matrix element. The delta function in Eq. (2.19) indicates that the difference between the initial and final energy ($E_e - E_h$) of the electron must be equal to the energy $\hbar\omega$ of the photon that induced the transition.

2.4 Gain Spectrum

Optical transitions can only occur between occupied initial states and empty final states with the same \mathbf{k} . If the number of downward transitions per second exceeds the number of upward transitions, there will be a net generation of photons, and optical gain can be achieved. The material gain g_{act} is calculated as [45],

$$g_{act}(\hbar\omega) = \left(\frac{1}{\hbar\omega} \right) \frac{\pi e^2 \hbar}{n_{act} \epsilon_0 c m_0^2} \sum_{c,v} \rho_{cv} |M_{cv}|^2 (f_c - f_v), \quad (2.21)$$

where n_{act} is the refractive index of the active region, ρ_{cv} is the joint-density-of-states, $f_c(f_v)$ is the electron (hole) occupation probability, and M_{cv} is the transition matrix element for interband transitions as defined by Eq. (2.20).

It is convenient to calculate the modal gain, g_{mod} in terms of g_{act} , the local gain in the active layers. This is the gain that would occur in a uniform active

medium having the same optical properties as the QWells. We can relate g_{act} to g_{mod} of a QWell by [44],

$$\frac{g_{mod}}{g_{act}} = \Gamma_{act}, \quad (2.22)$$

where Γ_{act} is known as the mode occupation factor of the active layers. For a QWire laser, considering the fact that not all regions within the active layer plane are active, g_{mod} and g_{act} are related by

$$\frac{g_{mod}}{g_{act}} = \Gamma_{act} \frac{W}{L_p}, \quad (2.23)$$

where L_p is the period of the QWire arrangement along the in-plane direction.

2.5 Linewidth Enhancement Factor

The carrier-induced coupling of the gain change to the refractive index change in the active region of a semiconductor laser is described by the linewidth enhancement factor (LEF) or α -factor. As such, it is a key parameter in many studies of semiconductor laser and amplifier performance under both continuous-wave (CW) operation and high-frequency modulation. Important characteristics dependent on α -factor include the laser linewidth, modulation-induced wavelength chirp, gain guiding and sensitivity to feedback. To explore the optimization conditions, it is thus important to investigate the dependencies of α -factor on the gain medium and structural properties. In addition, nonlinearities described by α -factor generate filamentation, which limits the performance of high-power semiconductor lasers. Thus, low- α operation is always desirable in practical devices.

In semiconductor lasers, the lasing transitions occur between two energy bands and this leads to asymmetry of the gain spectrum. When Hilbert-transformed, this spectrum produces a dispersion curve of refractive index with zero shifted from the gain peak frequency [34]. Since the gain varies with carrier density, the refractive index around the lasing frequency will also depend on the carrier density. It is well known that any change in the imaginary part of the susceptibility (gain or loss) will be accompanied by a corresponding change in its real part (refractive index) through the Kramers-Kronig relations [32]. The enhanced linewidth is attributed to the variation of the real refractive index n' with carrier density. Spontaneous emission induces phase and intensity changes in the laser

field. The restoration of the laser to its steady state intensity results in changes in the imaginary part of the refractive index $\Delta n''$. These changes are accompanied by the changes in the real part of the refractive index $\Delta n'$, which cause additional phase fluctuations and line broadening. α -factor, is expressed as [25],

$$\alpha = \frac{\Delta n'}{\Delta n''}. \quad (2.24)$$

Chapter 3

Calculation Procedure

In this chapter, procedures for calculating the device parameters, gain and α -factor are presented.

3.1 Device structure

Fig. (3.1) shows the schematic cross-sectional diagram of an InGaAsP vertically stacked multiple QWire structure under our consideration. The coordinate axes are also shown. The wire axes are along the crystallographic [110] directions. The crystal growth is along the [001] direction (z direction) for the structure. L_y and L_z are the width and the height of the QWire, respectively.

3.2 Material Properties of InGaAsP Systems

The laser structures considered in this work are made of the quaternary material system $\text{In}_{1-x}\text{Ga}_x\text{As}_y\text{P}_{1-y}$ grown on an InP substrate. This is the current material of choice for the fabrication of lasers for optical fibre communication, since the 1.3- μm and 1.55- μm wavelength range set by the optical properties of the silica fibres is easily accessed by this choice. This choice has obvious advantages, such as, suitability in the range of bandgaps and ease of fabrication. Moreover, it allows incorporation of a wide range of both compressive and tensile strain into the active layer. A disadvantage in having to deal with a quaternary mixed crystal system is that the material constants are not very well known; these are required for quantitative modeling of the design and engineering of working devices.

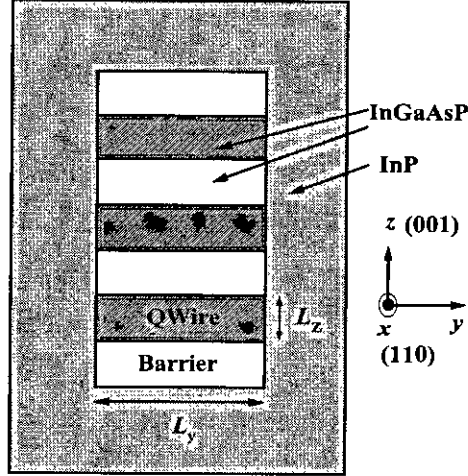


Figure 3.1: Cross-sectional schematic diagram of a vertical stack of multiple QWire structures.

In order to obtain various parameters for the $\text{In}_{1-x}\text{Ga}_x\text{As}_y\text{P}_{1-y}$ material system, a linear interpolation between parameters of relevant binary and ternary semiconductors are used. The material parameters of the binary and ternary semiconductors are listed in Table 3.1 [44].

The material constants of the quaternaries are, in general, a function of their composition (x and y) and, in principle, should be measured for each composition. Since, the quaternaries are aimed to lattice match the InP substrate, we regard the lattice matched quaternary as if it were composed of the ternary ($\text{In}_{0.532}\text{Ga}_{0.468}\text{As}$) and InP [44]. Thus:

$$\text{In}_{1-x}\text{Ga}_x\text{As}_y\text{P}_{1-y} = (\text{In}_{0.532}\text{Ga}_{0.468}\text{As})_z(\text{InP})_{1-z}, \quad (3.1)$$

where

$$z = y = x/0.468.. \quad (3.2)$$

All the material constants for the quaternary are linearly interpolated between these of InP and those of $\text{In}_{0.532}\text{Ga}_{0.468}\text{As}$ assuming Vegard's law [46]. Thus the material constants for the quaternaries are obtained using the following equation,

$$A^Q(x, y) = (1 - y)A^{\text{InP}} + yA^T + y(A^{\text{GaAs}} - A^{\text{InAs}})(x - 0.468y), \quad (3.3)$$

Table 3.1: Material Constants

Symbols	GaAs	InAs	InP	In _{0.532} Ga _{0.468} As
$E_g(300\text{K})$ eV	1.424	0.354	1.351	0.75
Δ_0 (eV)	0.341	0.371	0.110	0.356
m_e (emu)	0.0665	0.023	0.079	0.041
γ_1	6.790	19.67	4.95	11.01
γ_2	1.924	8.37	1.65	4.18
γ_3	2,782	9.29	2.35	4.84
a_g (eV)	-9.77	-6.0	-6.35	-7.76
a_c (eV)	-7.1	-5.4	-5.35	-6.2
b_v (eV)	-1.7	-1.8	-2.0	-1.75
d_v (eV)	-4.55	-3.6	-4.2	-4.04
E_p (eV)	28.8	22.2	20.4	25.3
$C_{11}(\times 10^{11} \text{ dyn/cm}^2)$	11.81	8.329	10.22	10.08
$C_{12}(\times 10^{11} \text{ dyn/cm}^2)$	5.38	4.53	5.76	4.98
$a(300^0\text{K})$ Å	5.6532	6.0583	5.8587	5.8687

where A is one of the material constants, Q stands for the quaternary, and T stands for the lattice-matched ternary. For the quaternary bandgap, however, we use parabolic interpolation, to account for the bowing of the bandgap upto second order [47]:

$$E_g^Q(x, y) = E_g^{\text{InP}} + 0.672x - 1.091y + 0.758x^2 + 0.101y^2 + 0.111xy - 0.580x^2y - 0.159xy^2 + 0.268x^2y^2. \quad (3.4)$$

For the lattice constant, the following interpolation formula is used [46]:

$$a^Q(x, y) = a^{\text{InP}} + 0.189y - 0.418x + 0.013xy. \quad (3.5)$$

Lattice parameters and the bandgap energy for InGaAsP quaternary material systems are related by the curves shown in Fig. 3.2 [46]. The misfit strain for the quaternary is defined as

$$e_0 = \frac{a^{\text{InP}} - a^Q}{a^Q}. \quad (3.6)$$

3.3 Analytical Expressions for Strain Distribution

Strained QWires use a material which has a different native lattice constant than the surrounding barrier material. In this case, one or both of the materials adjusts

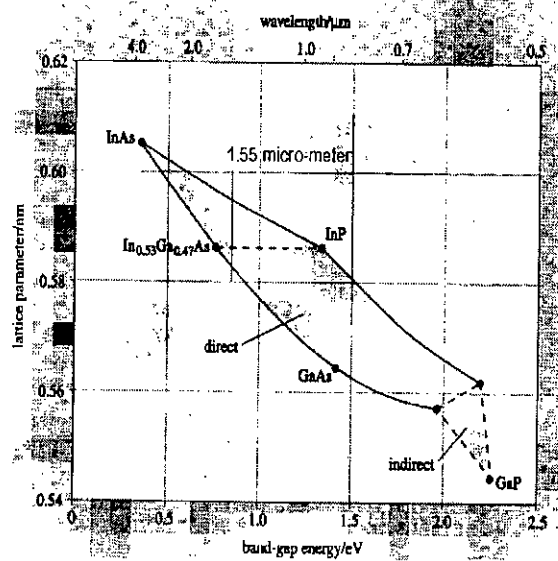


Figure 3.2: Lattice parameter vs bandgap energy for the binary and ternary material system.

its lattice constants to match the other and an equilibrium situation is reached.

To obtain the strain tensor components e_{ij} ($i, j = x, y, z$), we follow an analytical approach [20]. There are also other methods, such as finite-element method (FEM), finite difference method (FDM), etc., available to calculate the strain distributions. FEM calculations can be cumbersome, however, because it is necessary to carefully divide the structure into fine meshes so that consistent results are obtained. The accuracy of the final results are also questionable in this method, particularly, in regions where the strain is varying rapidly because of not embedding the QWire in truly infinite matrix. Analytical expressions, on the other hand, give a quick and accurate method of obtaining the strain fields and allow an insight into the physics of the problem provided the materials can be assumed to be continuous, linear and isotropic obeying Hooke's laws.

For the structure shown in Fig. 3.3, the initial strain in the x , y and z directions is e_0 within the layer and zero outside. The dimension of the structure

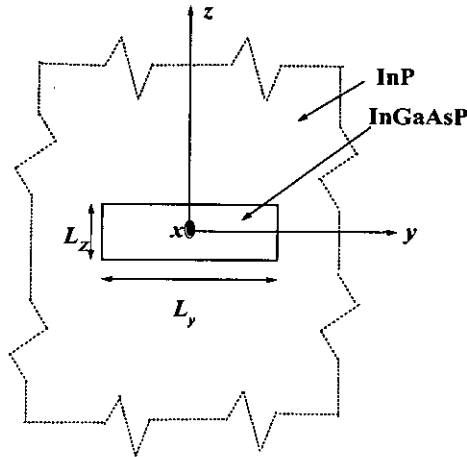


Figure 3.3: Cross-sectional schematic diagram of a buried strained layer. Important dimension and the coordinate axes are indicated.

in x direction is assumed to be very large (ideally infinite) compared to L_y or L_z so that a two-dimensional analysis with plane strain condition is appropriate. The analysis starts with the solution for a finite circular inclusion in two dimensions which forms a cylindrical inclusion when extended into the third dimension. The cylindrical inclusion of radius r exerting a pressure P yields stress fields outside the cylinder which are easily determined [20]. Dividing the stresses by πr^2 give the stress components per unit area of inclusion:

$$\begin{aligned}\sigma_{yy}^{cyl} &= \frac{P}{\pi} \frac{y^2 - z^2}{(y^2 + z^2)^2}, \\ \sigma_{zz}^{cyl} &= \frac{P}{\pi} \frac{z^2 - y^2}{(y^2 + z^2)^2}, \\ \sigma_{yz}^{cyl} &= \frac{2P}{\pi} \frac{yz}{(y^2 + z^2)^2}.\end{aligned}\tag{3.7}$$

The technique is based on a 2-D Green's function for the stress field. The stress fields for the n th strained layer illustrated in Fig. 3.3 are obtained by integrating the stress field per unit area of inclusion for the cylindrical inclusion over a rectangle of length L_y and height L_z , thus

$$\sigma^n(y, z) = \int_{(L_y)} \int_{(L_z)} \sigma^{cyl}(y - y_0, z - z_0) dy_0 dz_0,\tag{3.8}$$

generating the results,

$$\begin{aligned}\sigma_{yy}^n(y, z) &= \frac{P}{\pi} \left[\tan^{-1} \left(\frac{l_y - y}{l_z - z} \right) + \tan^{-1} \left(\frac{l_y + y}{l_z - z} \right) \right. \\ &\quad \left. + \tan^{-1} \left(\frac{l_y - y}{l_z + z} \right) + \tan^{-1} \left(\frac{l_y + y}{l_z + z} \right) \right], \\ \sigma_{zz}^n(y, z) &= \frac{P}{\pi} \left[\tan^{-1} \left(\frac{l_z - z}{l_y - y} \right) + \tan^{-1} \left(\frac{l_z - z}{l_y + y} \right) \right. \\ &\quad \left. + \tan^{-1} \left(\frac{l_z + z}{l_y - y} \right) + \tan^{-1} \left(\frac{l_z + z}{l_y + y} \right) \right], \quad (3.9)\end{aligned}$$

$$\begin{aligned}\sigma_{yz}^n(y, z) &= \frac{P}{2\pi} [\ln |(l_y + y)^2 + (l_z - z)^2| + \ln |(l_y - y)^2 + (l_z + z)^2| \\ &\quad - \ln |(l_y - y)^2 + (l_z - z)^2| - \ln |(l_y + y)^2 + (l_z + z)^2|].\end{aligned}$$

where $l_y = L_y/2$ and $l_z = L_z/2$. These are the stress fields associated with the n th strained layer of dimension $L_y \times L_z$ buried in an infinite medium. The principle of superposition is applied to calculate the stress field at a point due to multiple strained layers.

The stress components given in Eq. (3.9) are used to determine the strain components using Hooke's laws. Here, e_{xx} is equal to the misfit strain, e_0 , within the strained layer, but e_{xx} is equal to zero outside this region. The Hooke's law relations for plane strain for the n th strained layer, therefore, become [20]

$$\begin{aligned}e_{yy}^n(y, z) &= \frac{1}{E} [(1 - \nu^2)\sigma_{yy}^n(y, z) - \nu(1 + \nu)\sigma_{zz}^n(y, z)] - \nu e_0(y, z), \\ e_{zz}^n(y, z) &= \frac{1}{E} [(1 - \nu^2)\sigma_{zz}^n(y, z) - \nu(1 + \nu)\sigma_{yy}^n(y, z)] - \nu e_0(y, z), \quad (3.10) \\ e_{yz}^n(y, z) &= \frac{2(1 + \nu)}{E} \sigma_{yz}^n(y, z),\end{aligned}$$

where $e_0(y, z)$ is the misfit of the material at position (y, z) , E is Young's modulus and ν is the Poisson's ratio.

Finally, an expression for the constant P/π in terms of the lattice mismatch, e_0 defined in Eq. (3.6), is found [20]. Eq. (3.9) gives the in-plane stress at the centre of a long thin layer ($l_y/l_z \rightarrow \infty$) as $2P$. The Hooke's law expression then yields

$$P = \frac{e_0 E}{2(1 - \nu)}. \quad (3.11)$$

3.4 Calculation of Electronic States

The heterostructure is composed of several regions, each of a definite composition and/or uniform state of strain. In such a situation, the parameters in the Hamiltonian matrix defined in Eq. (2.5) are constants in each region but differ from region to region. Also in such a situation, the question of how to match the envelope functions in one region to those of the next region arises. The simple prescription for automatically including the correct boundary conditions into the formulation of the problem was studied from [44]. That prescription is as follows: In every terms of Eqs. (2.7) and (2.8) in which a material parameter and a derivative both appear, one has to make the replacement

$$\begin{aligned} Q \frac{\partial}{\partial x_\mu} &\rightarrow \frac{1}{2} \left[Q(\mathbf{r}) \frac{\partial}{\partial x_\mu} + \frac{\partial}{\partial x_\mu} Q(\mathbf{r}) \right], \\ Q \frac{\partial}{\partial x_\mu} \frac{\partial}{\partial x_\nu} &\rightarrow \frac{1}{2} \left[\frac{\partial}{\partial x_\mu} Q(\mathbf{r}) \frac{\partial}{\partial x_\nu} + \frac{\partial}{\partial x_\nu} Q(\mathbf{r}) \frac{\partial}{\partial x_\mu} \right], \end{aligned} \quad (3.12)$$

where $Q(\mathbf{r})$ is any real material parameter or strain tensor component.

The spatial dependence of the parameter $Q(\mathbf{r})$ is expressed in terms of step functions for the interfaces i.e., for an interface at $x = x_0$, where material A is to the left side of the interface and B is to the right side:

$$Q(x) = Q_A + (Q_A - Q_B)\Theta(x - x_0)$$

where $\Theta(x)$ is the unit step function.

The 8×8 matrix obtained in this way has elements $H_{nn'}(\mathbf{r}, \nabla)$ and the eight coupled differential equations are

$$\sum_{n'=1}^8 H_{nn'}(\mathbf{r}, \nabla) F_{n'}(\mathbf{r}) = E F_n(\mathbf{r}). \quad (3.13)$$

These equations are solved by applying the so-called eigenfunction expansion method [44]. Thus, for the QWire structure, the above envelope function F , for a particular wave vector k_x along the QWire axis, is expressed in terms of a 2-D Fourier series

$$F_n(\mathbf{r}) = \sum_{lm}^{\infty} F_n(l, m, k_x) \phi_{lmk_x}(x, y, z), \quad (3.14)$$

with the basis function ϕ given by

$$\phi_{lmk_x}(x, y, z) = (L_y L_z)^{-\frac{1}{2}} \exp \left[i2\pi \left(l \frac{y}{L_y} + m \frac{z}{L_z} \right) + ik_x x \right], \quad (3.15)$$

and for the QWell structure, it is expressed, similarly, in terms of a 1-D Fourier series

$$F_n(\mathbf{r}) = \sum_m^\infty F_n(m, k_x, k_y) \phi_{mk_x k_y}(x, y, z), \quad (3.16)$$

with the basis function ϕ given by

$$\phi_{mk_x k_y}(x, y, z) = (L_z)^{-\frac{1}{2}} \exp \left[i2\pi \left(m \frac{z}{L_z} \right) + ik_x x + ik_y y \right]. \quad (3.17)$$

In order to convert the differential Eq. (3.13) for a QWire into a set of algebraic equations, we insert the expansion given in Eq. (3.16) into Eq. (3.13), multiply by $\phi_{lmk_x}^*(x, y, z)$ and integrate over the region $L_y L_z$. The resultant matrix eigenvalue equation has the form:

$$\sum_{n'l'm'} H_{nn'}(l', m', l, m) F_{n'}(l', m') = E F_n(l, m), \quad (3.18)$$

where the matrix elements $H_{nn'}(l', m', l, m)$ are given by:

$$H_{nn'}(l', m', l, m) = \int dy dz \phi_{l'm'}^*(y, z) H_{nn'}(\mathbf{r}, \nabla) \phi_{lm}(y, z). \quad (3.19)$$

All matrix elements can be evaluated analytically if each interface is perpendicular to one or another coordinate axis.

Formally, for our QWire structure, Eq. (3.19) may be expressed as

$$H_{nn'}(l', m', l, m, k_x) = \int_{(L_y)} \int_{(L_z)} dy dz \phi_{l'm'}^*(y, z) H_{nn'} \left(y, z, k_x, \frac{\partial}{\partial y}, \frac{\partial}{\partial z} \right) \phi_{lm}(y, z). \quad (3.20)$$

For the QWell structure, similar explanation can be obtained. The matrix elements for the QWell structure is now given by

$$H_{nn'}(m', m, k_x, k_y) = \int_{(L_z)} dz \phi_{m'}^*(z) H_{nn'} \left(z, k_x, k_y, \frac{\partial}{\partial z} \right) \phi_m(z). \quad (3.21)$$

When constructing the matrix H , there are two useful checks on the numerical work. The first check is that the matrix H is Hermitian:

$$H_{nn'}(l', m', l, m) = H_{n'n}(l, m, l', m')^*. \quad (3.22)$$

The second check is that the matrix H expressed in a Kramers basis (a basis containing $2N$ functions arranged so that the $(j + N)$ -th function is the time-reverse conjugate of the j -th function) must also have the form of Eq. (2.5). In constructing the Kramers basis for the matrix H , we note that the original 8-function basis is a Kramers basis and that $\phi_{-l,-m}(y, z)$ is the time reverse conjugate of $\phi_{l,m}(y, z)$.

The integral in Eqs. (3.20) and (3.21) extend over all spatial regions. In each region, the material parameters are constant. The integrands also contain delta functions at each internal interface. The strength of these delta functions is governed by the discontinuity of the material parameters at the interface. There are thus two types of terms contained in Eqs. (3.20) and (3.21): bulk terms (integrals over the interior of the region), and the surface terms (the delta-function parts). The contributions of each region and of each internal interface are additive. Our program calculates the matrix elements region by region and interface by interface and adds them together.

For the QWire structure, all the bulk contributions to the matrix elements contain integrals of the form:

$$I_{l'm'tm}^R = \frac{1}{L_y L_z} \int_{R_{L_y}}^{R_{R_y}} \int_{R_{L_z}}^{R_{R_z}} dy dz e^{-i\left(l' \frac{y}{L_y} + m' \frac{z}{L_z}\right)} e^{i\left(l \frac{y}{L_y} + m \frac{z}{L_z}\right)}, \quad (3.23)$$

while for the QWell structure, the integral takes the form:

$$I_{m'm}^R = \frac{1}{L_z} \int_{R_{L_z}}^{R_{R_z}} dz e^{-i\left(m' \frac{z}{L_z}\right)} e^{i\left(m \frac{z}{L_z}\right)}, \quad (3.24)$$

where R_{L_y} , R_{L_z} are the left side edges of the zone R along y , z directions, respectively and R_{R_y} , R_{R_z} are its right side along the same directions. Analytical solutions for these integral are given as follows. For the QWire structure,

$$I_{l'm'tm}^R = \begin{cases} \frac{1}{L_y L_z} (R_{R_y} - R_{L_y})(R_{R_z} - R_{L_z}) & ; l = l', m = m' \\ \frac{1}{i L_y L_z} \left[\frac{L_y}{l - l'} \left(e^{i \frac{l-l'}{L_y} R_{R_y}} - e^{i \frac{l-l'}{L_y} R_{L_y}} \right) \right. \\ \left. + \frac{L_z}{m - m'} \left(e^{i \frac{m-m'}{L_z} R_{R_z}} - e^{i \frac{m-m'}{L_z} R_{L_z}} \right) \right] & ; l \neq l', m \neq m', \end{cases} \quad (3.25)$$

and for the QWell structure,

$$I_{m',m}^R = \begin{cases} \frac{R_{R_z}}{R_{L_z}} L_z, & m = m' \\ \frac{i}{m' - m} \left(e^{i \frac{m-m'}{L_z} R_{R_z}} - e^{i \frac{m-m'}{L_z} R_{L_z}} \right), & m \neq m'. \end{cases} \quad (3.26)$$

The spatial variables x , y and z are along the QWire coordinate system as shown in Fig. (3.3). Since the element of the Hamiltonian are defined in terms of the crystallographic coordinates while ϕ and the strain components are expressed in terms of QWire coordinates, QWire coordinate system is rotated by an appropriate transformation matrix to orient it along the crystallographic axes.

After completing the construction of the matrices given in Eqs. (3.20) for the QWire, they are diagonalized to get the eigenenergies E . Solutions of Eq. (3.13) also gives the Fourier coefficients $F_n(l, m, k_x)$. All the eigenvalues and eigenstates within the defined range are stored and a new k_x point is chosen and the whole procedure is repeated to complete the computation of a set of dispersion curves for the QWire.

3.5 Calculation of Transition Matrix Elements

For evaluating the transition rate between initial state $\Psi_i(\mathbf{r})$ and a final state $\Psi_f(\mathbf{r})$ of the unperturbed Hamiltonian, we need to calculate the term:

$$|\langle \Psi_f(\mathbf{r}) | H_{rad} | \Psi_i(\mathbf{r}) \rangle|^2 = A_0^2 \left(\frac{e}{2m_0c} \right)^2 M_{f,i}. \quad (3.27)$$

Here, $M_{f,i}$ is known as the optical matrix element and it is given by [44],

$$|M_{f,i}|^2 = |\langle \psi_f(\mathbf{r}) | \hat{e} \cdot \frac{\hbar}{i} \nabla | \psi_i(\mathbf{r}) \rangle|^2, \quad (3.28)$$

where \hat{e} is a unit vector in the direction of the electric field of the radiation. The approach is general enough so that i and f may both be within the valence band (intravalence band transition), conduction band (intraconduction band transition) or one may belong to the valence band and the other to the conduction band (interband transition). Now, substituting

$$\begin{aligned} \psi_{i,f}(\mathbf{r}) &= \sum_{n=1}^8 F_n^{i,f}(\mathbf{r}) U_n(\mathbf{r}) \\ &= \sum_{n=1}^8 \sum_{jlm} F^{i,f}(j, l, m) \phi_{jlm}(x, y, z) U_n(\mathbf{r}), \end{aligned} \quad (3.29)$$

into Eq. (3.28), we have

$$\begin{aligned}
|M_{f,i}|^2 &= \left| \sum_{n,n'=1}^8 \sum_{jlm} \sum_{j'l'm'} F_n^{j*}(j,l,m) F_{n'}^{j'}(j',l',m') \right. \\
&\quad \cdot \int \phi_{jlm}^*(x,y,z) U_n^*(\mathbf{r}) \hat{e} \\
&\quad \left. \cdot \frac{\hbar}{i} \nabla \phi_{j'l'm'}(x,y,z) U_{n'}(\mathbf{r}) dx dy dz dr \right|^2. \tag{3.30}
\end{aligned}$$

If we make use of the fact that the envelope functions vary relatively slowly over regions the size of a unit cell, then the integral in Eq. (3.30) can be written as

$$\begin{aligned}
\int \phi_{jlm}^*(x,y,z) U_n^*(\mathbf{r}) \hat{e} \cdot \frac{\hbar}{i} \nabla \phi_{j'l'm'}(x,y,z) U_{n'}(\mathbf{r}) dx dy dz dr \\
\cong \int \phi_{jlm}^*(x,y,z) \phi_{j'l'm'}(x,y,z) dx dy dz \\
\quad \cdot \int_{\Omega(xyz)} U_n^*(\mathbf{r}) \hat{e} \cdot \frac{\hbar}{i} \nabla U_{n'}(\mathbf{r}) d\mathbf{r} \\
+ \int \phi_{jlm}^*(x,y,z) \hat{e} \cdot \frac{\hbar}{i} \nabla \phi_{j'l'm'}(x,y,z) dx dy dz \\
\quad \cdot \int_{\Omega(xyz)} U_n^*(\mathbf{r}) U_{n'}(\mathbf{r}) d\mathbf{r}. \tag{3.31}
\end{aligned}$$

The first integral over $\Omega(xyz)$ in Eq. (3.31) is actually a sum of three integrals, each being multiplied by a component of \hat{e} . Each of the three is proportional to the optical matrix P or else vanishes unless n, n' and the component of ∇ are related in a way so that both n and n' must refer to the same direction of spin, n must be in the conduction band while n' must be in the valence band or vice versa and finally the component of ∇ must be the same as the label (x, y, z) of the valence band state. The second integral over $\Omega(xyz)$ is the overlap of two Bloch waves. It vanishes unless $n = n'$.

3.6 Calculation of Reduced Density of States and Quasi-Fermi Energies

Fermi's golden rule gives the transition rate for a single pair of conduction and valence band states. We know that many k states exist in both conduction and valence bands. To find the total transition rate, we must sum Eq. (2.19) over all transition pairs that are allowed. In our work, we only consider undoped material such that band-to-band transitions dominate, allowing us to assume

strict k -selection rules. Thus, only vertical transitions in k space are allowed, and we can simply sum over all N_s electronic states in either bands. The total transition rate per unit volume is then given (in units of $s^{-1}cm^{-3}$) by

$$\begin{aligned} W_{c \rightarrow v} &= \frac{1}{V} \int W_{e \rightarrow h} dN_s = \int W_{e \rightarrow h} \frac{1}{V} \frac{dN_s}{dk} dk \\ &= \frac{2\pi}{\hbar} \int |H_{rad(eh)}|^2 \delta(E_{eh} - \hbar\omega) \rho(k) dk, \end{aligned} \quad (3.32)$$

where, by definition,

$$\rho(k) = \frac{1}{V} \frac{dN_s}{dk}, \quad (3.33)$$

and we have introduced the transition energy, $E_{eh} \equiv E_e - E_h$, into the delta function. Letting $x = E_{eh} - \hbar\omega$, the integral becomes

$$\begin{aligned} W_{c \rightarrow v} &= \frac{2\pi}{\hbar} \int |H_{rad(eh)}|^2 \delta(x) \rho(k) \frac{dx}{dE_{eh}/dk} \\ &= \frac{2\pi}{\hbar} |H_{rad(eh)}|^2 \left[\frac{\rho(k)}{dE_{eh}/dk} \right]_{E_{eh}=\hbar\omega}. \end{aligned} \quad (3.34)$$

The term in brackets is defined as the combined or joint or reduced density of states (RDOS).

Another important parameter is the carrier density required to achieve a given quasi-Fermi level separation. The carrier density in a given band can be found for a given quasi-Fermi level by integrating the density of states multiplied by the occupation probability over the entire band. For nonparabolic bands, for example, in the valence band of a QWell, where the subband structure is far from parabolic, we find the carrier density by numerically integrating over k space, because k -states are always uniformly in k space, independent of how complicated the energy bands become. For this case, we have [45],

$$\begin{aligned} P &= 2 \sum \int_0^{k_{max}} \rho^{mD}(\mathbf{k}) [1 - f_v(\mathbf{k})] d\mathbf{k}, \\ N &= 2 \sum \int_0^{k_{max}} \rho^{mD}(\mathbf{k}) f_c(\mathbf{k}) d\mathbf{k}, \end{aligned} \quad (3.35)$$

where $m= 1, 2$ for QWell and QWire, respectively and k_{max} represents some numerical limit beyond which the contribution to the integral can be neglected. The sum is taken over all quantized subbands within the valence band (including both HH and LH bands) and the conduction band, respectively. The occupation

probabilities are given by

$$\begin{aligned} f_c(\mathbf{k}) &= \frac{1}{1 + \exp\left(\frac{E_c(\mathbf{k}) - E_{fc}}{k_B T}\right)}, \\ f_v(\mathbf{k}) &= \frac{1}{1 + \exp\left(\frac{E_v(\mathbf{k}) - E_{fv}}{k_B T}\right)}, \end{aligned} \quad (3.36)$$

where E_{fc} and E_{fv} are the quasi-Fermi levels and k_B is the Boltzmann constant. We find E_{fc} and E_{fv} from the requirement that the average carrier density in QWire have specified values N and P .

3.7 Calculation of Gain Spectrum

To evaluate g_{act} in Eq. (2.21), we first compute the band structure associated with the QWire. We calculate all conduction band and valence band dispersion curves or minibands that are likely to be occupied with electrons or holes, respectively. Only these minibands can contribute to emission and, hence, to gain. We do this for a number of points (e.g., 81) in k space. Then, we calculate the matrix elements of each polarization for all transitions between these states. The Fermi levels are then set in an iterative procedure by varying them until the specified carrier densities are reached. Once the Fermi levels are established, $g_{act}(\hbar\omega)$ can be evaluated with Eq. (2.21). The most time-consuming step is to solve the eigenvalue problem for all energy levels and wavefunctions. Once this is done, it is relatively quick to compute the gain spectra for a set of carrier densities.

In deriving the expression for the material gain, we have assumed that an electron in a conduction band state would remain in that state forever if it weren't for interactions with photons, i.e., the energy of the state is sharp. In reality, interactions with phonons and other electrons from time to time scatter the electron into another conduction band state. Therefore, the lifetime of a given state is not infinite. In fact, it is presently believed that, on average, approximately every 0.1 ps an electron (or hole) is bumped into a new state [45]. If we assume that the state decays exponentially with time, then the Fourier energy spectrum necessary to construct the time-dependent state has a Lorentzian lineshape, and hence the energy of each state (and each transition) is no longer sharp but has

an energy spread over a range of ΔE on each side of the expected energy of the state (or transition). This means that an incoming photon with energy $\hbar\omega$ will not only interact with transitions given by $E_{eh} = \hbar\omega$, but also with transitions within an energy spread $E_{eh} \approx \hbar\omega \pm \Delta E$.

To include the spectral broadening of each transition, we convolve the expression for material gain with some spectral lineshape function over all transition energies E_{eh} to obtain [45],

$$G_{act}(\hbar\omega) \equiv \int g_{act}(\hbar\omega)L(E_{eh})dE_{eh}, \quad (3.37)$$

where

$$L(E_{eh}) \equiv \frac{1}{\pi} \frac{\hbar/\tau_{in}}{(E_{eh} - \hbar\omega)^2 + (\hbar/\tau_{in})^2}, \quad (3.38)$$

where $g_{act}(\hbar\omega)$ is taken directly from Eq. (2.21). $L(E_{eh})$ is a normalized Lorentzian lineshape function and τ_{in} is the intraband relaxation time, or simply the lifetime of each state, and is about 0.1 ps [45] in bulk material. $G_{act}(\hbar\omega)$ is now spectrally smoothed gain.

3.8 Calculation of Linewidth Enhancement Factor

The complex refractive index in the vicinity of the absorption edge can be written as

$$n = n_0 + \Delta n' + i\Delta n'', \quad (3.39)$$

where $\Delta n' + i\Delta n''$ is the part of the refractive index that changes with injected carrier density. The complex wave vector $k = k_0 + \Delta k' + i\Delta k''$ is related to the refractive index by [32],

$$(k_0 + \Delta k' + i\Delta k'')^2 = \left(\frac{\omega^2}{c^2}\right) (n_0 + \Delta n' + i\Delta n'')^2. \quad (3.40)$$

Therefore, the change in wave vector with changes in injected carrier density is found by equating terms in Eq. (3.40) and neglecting terms of second order,

$$(\Delta k' + i\Delta k'') = \left(\frac{\omega^2 n_0}{c^2 k_0}\right) (\Delta n' + i\Delta n''). \quad (3.41)$$

To a good approximation, n_0 is real and constant and $k_0 = \omega/cn_0$. Writing $\omega/c = 2\pi E$, where E is the photon energy in cm^{-1} , and using the relation between the imaginary part of k and gain

$$g = -2k'' \quad (3.42)$$

We have, from Eqs. (3.41) and (3.42)

$$\Delta n'' = -\frac{\Delta g}{4\pi E} \quad (3.43)$$

The real and imaginary parts of the dielectric constant are related by the Kramers-Kronig (KK) dispersion relations which is as shown below:

$$f_1(x) = \frac{2}{\pi} \int_0^\infty \frac{x' f_2(x') dx'}{x'^2 - x^2}, \quad (3.44)$$

where $f_1(x)$ and $f_2(x)$ are real and imaginary parts of some complex function $f(x)$, respectively. Changes in the dielectric constant are also related by the KK relations. In the approximation that n_0 is constant, $\Delta n'$ and $\Delta n''$ are related by the KK relations, we have [32],

$$\begin{aligned} \Delta n'(E) &= \frac{2}{\pi} P \int_0^\infty \frac{E' \Delta n''(E') dE'}{E'^2 - E^2} \\ &= -\frac{1}{2\pi^2} P \int_0^\infty \frac{\Delta g(E') dE'}{E'^2 - E^2}, \end{aligned} \quad (3.45)$$

where P indicates taking the principal value of the integral. This integral is difficult to compute numerically because of the singularity at $E = E'$. This singularity can be avoided by using a transformation suggested by Henry *et al.* [32]. We subtract and add $\Delta g(E)$ to the integrand. Then,

$$\Delta n'(E) = -\frac{1}{2\pi^2} P \int_0^\infty \frac{1}{E' + E} \left(\frac{\Delta g(E') - \Delta g(E)}{E' - E} \right) dE' - \frac{\Delta g(E)}{2\pi^2} P \int_0^\infty \frac{dE'}{E'^2 - E^2}. \quad (3.46)$$

It is easily demonstrated that the second integral is zero. The integrand of the first integral is no longer singular. As $E' \rightarrow E$, the integrand approaches the finite limit $(2E)^{-1} d\Delta g(E)/dE$. Once the change in the real and imaginary parts of the refractive index is known, spectral LEF (α -factor) can be computed from Eq. (2.24) [25].

Chapter 4

Results and Discussions

The results of the numerical calculations for the QWire devices are presented in this chapter. Effects of non-parabolicity due to material properties, quantum-confinement and elastic strain relaxation are incorporated in the calculation. The detail of the device structures are given in Fig. (3.1). The initial wafer consists of multiple layers of $\text{In}_{1-x}\text{Ga}_x\text{As}_y\text{P}_{1-y}$ biaxially CS quantum-well layers ($\lambda_g = 1.58\mu\text{m}$), and TS or LM barriers grown on a (001) InP substrate. In all our analyses, the thickness of the well in the crystal growth direction $L_z = 7\text{ nm}$, and the thickness of the barriers $L_B = 12\text{ nm}$. The lattice-misfit strain in QWire region is 1.07% compressive. The α -factor of QWire and QWell lasers are calculated and compared to identify the improvement caused by the additional carrier-confinement in QWires. Finally, effects of variation of device parameters, i.e., QWire width, strain, multi-well stack, etc. on the α -factor are investigated which allows optimizing device design to minimize the α -factor.

4.1 Dispersion relationships for QWires

The dispersion relationships of the lowest two conduction and the highest three valence band sub-levels in 10-nm and 20-nm-wide QWires are presented in Fig. 4.1(a-c) and (d-f), respectively, while the dispersion relationships of the highest three valence band sub-levels in 30-nm and 50-nm-wide QWires are depicted in Fig. 4.2(a-c) and (d-f), respectively. The calculation procedures for the dispersion relationships of the QWires are presented in Section 3.4. LM, 0.15% TS and 0.6% TS barriers are considered.

Table 4.1: Comparison of key dispersion relationship parameters for 10-, 20-, and 30-nm wide QWires as shown in Figs. 4.1 and 4.2

	LM Barriers			0.15% TS Barriers			0.6% TS Barriers		
	10 nm QWire	20 nm QWire	30 nm QWire	10 nm QWire	20 nm QWire	30 nm QWire	10 nm QWire	20 nm QWire	30 nm QWire
m_{h1}/m_0	0.2708	0.1854	0.1604	0.2060	0.1564	0.1392	0.1247	0.1053	0.0982
$\Delta E_{h12}(\text{meV})$	28.49	26.54	14.40	28.99	25.27	13.90	30.73	21.97	12.41
$E_0(\text{meV})$	865.53	820.36	807.97	862.89	817.79	805.39	851.70	806.56	794.34

It is found that for LM barriers, the nonparabolicity of the highest hole subband is strong near the zone centre due to band mixing. We also note that the band mixing in the excited hole subbands is stronger in the 10-nm QWire. Table 4.1 lists the values of the zone-centre effective mass of the highest hole subband m_{h1} , zone-centre separation between the highest two hole subbands ΔE_{h12} , and the fundamental electron-hole transition energy E_0 for the three QWires extracted from Figs. 4.1 and 4.2. For all the QWires, as expected, m_{h1} decreases with suppression of strain relaxation. For the 20- and 30-nm QWires, strain relaxation increases ΔE_{h12} whereas the opposite is true for the 10-nm QWire. The separation between the highest two valence subbands at the zone-centre decreases rapidly with increasing wire width for both the LM and TS barriers. These results demonstrate the complex interactions between strain relaxation and quantum confinement effects.

4.2 Gain Characteristics

In quantifying the gain, we need to know the number of transitions that will occur per second in the device in response to a given flux of photons in a given optical mode. Calculated transition matrix elements for ground state transitions M_{11} for transverse electric (TE) polarization with the electric field along the wire axis ($TE_{||}$) in a 20-nm wide QWire for LM and two types of TS barriers as well as for different number of quantum well layers are presented in Fig. 4.3(a) and (b), respectively. The procedures for calculating the transition matrix elements are described in Section 3.5. Results indicate that with an increase in the barrier

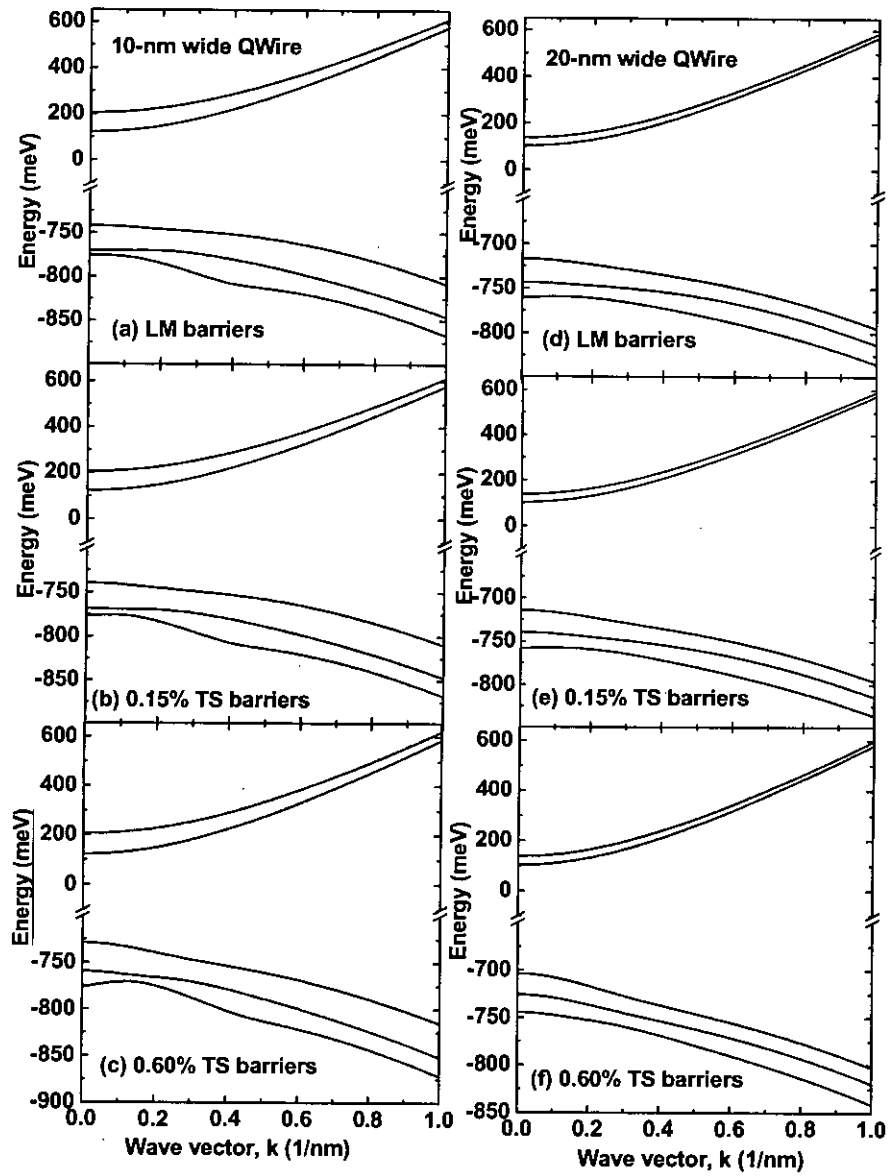


Figure 4.1: Dispersion relationships for the two lowest conduction and the three highest hole subbands in (a-c) 10-nm and (d-f) 20-nm wide QWires calculated for three different types of barriers.

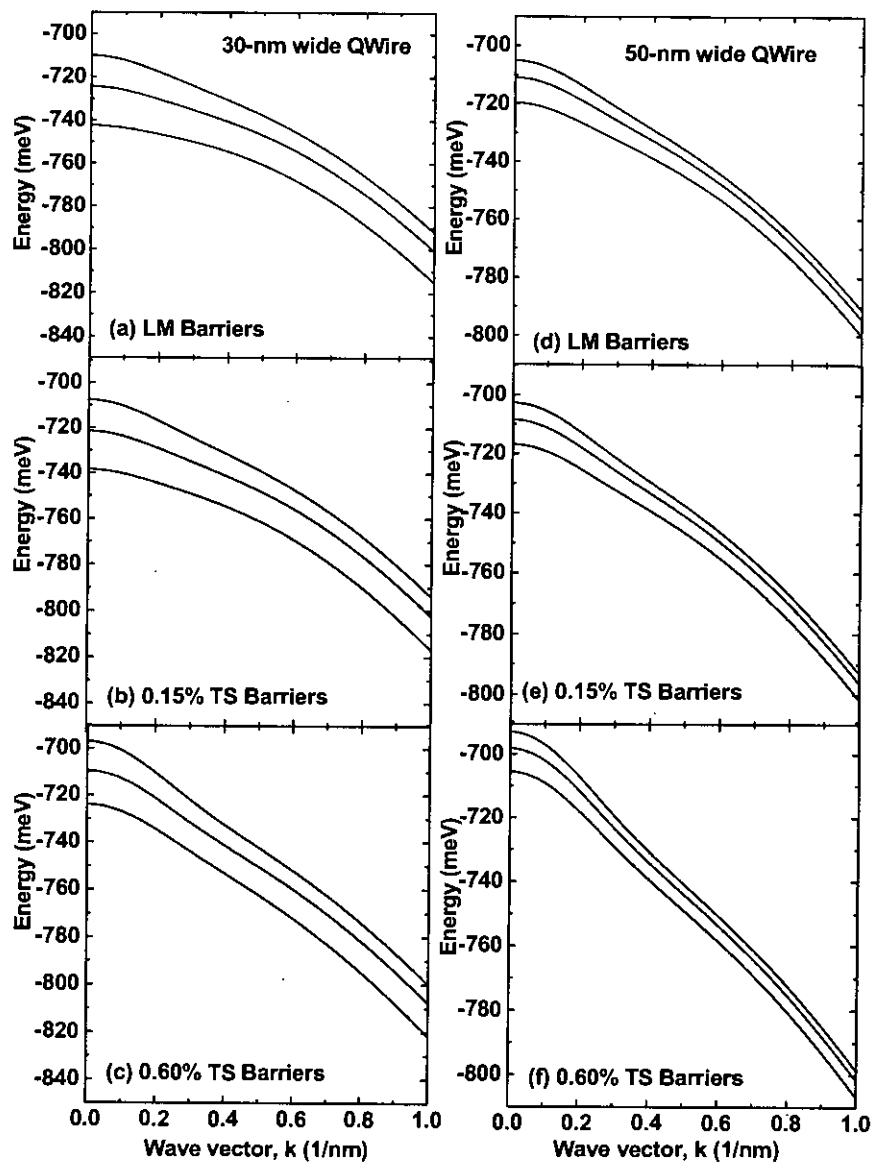


Figure 4.2: Dispersion relationships for the three highest hole subbands in (a-c) 30-nm and (d-f) 50-nm wide QWires calculated for three different types of barriers.

TS, transition strength is increased for the 1-1 transition. This is due to the fact that TS barriers suppress elastic strain relaxation which in turn makes the highest valence band level more HH like. It is seen in Fig. 4.3(b) that multiple-layer QWire shows less transition strength compared to the single-layer QWire due to more pronounced strain relaxation in multiple-layer QWires.

Fig. 4.4 presents the material gain spectra in a 20-nm and a 30-nm wide QWire as a function of the photon energy for LM and two types of TS barriers. The changes in the absorption characteristics of the material band edge from high absorption to high gain as a function of carrier density are clearly seen in the figure. The peaks in the gain/absorption spectra arise from the various sub-band transitions that maintain the k-selection rules. In all the cases, the peak gain is dominated by the 1-1 transitions for small carrier densities. However, for very high carrier densities, in wider wires, contributions to the gain from the 2-2 transitions become significant as is depicted from Fig. 4.4(d-f). It is also clear from the figures that QWire structures with highly SC barriers exhibit higher peak gain for a particular carrier density due to their relatively higher transition strength as is shown in Fig. 4.3(a).

Fig. 4.5 shows the peak material gain G as a function of the injected carrier density for 10-nm, 20-nm, 30-nm and 50-nm wide QWires. Both TS and LM barriers are considered. For all the QWires, G is the highest for the structures with 0.60% TS barriers and decreases with decreasing TS in barriers. These results can also be explained in terms of the strain relaxation dependence of the transition matrix elements as presented in Fig. 4.3(a). We also observe that when SC barriers are used, the transparency carrier density is reduced for all the wire widths. This is due to the fact that when strain relaxation is suppressed by SC barriers, effective mass of the highest hole subband is reduced (Table 4.1). This reduces the band edge hole density of states which, in turn, reduces the transparency carrier density. A feature worth noting is that for LM barriers, below transparency carrier density, the gain (actually absorption) shows some ripple. It will be shown later that this ripple has important consequences on the α -factor.

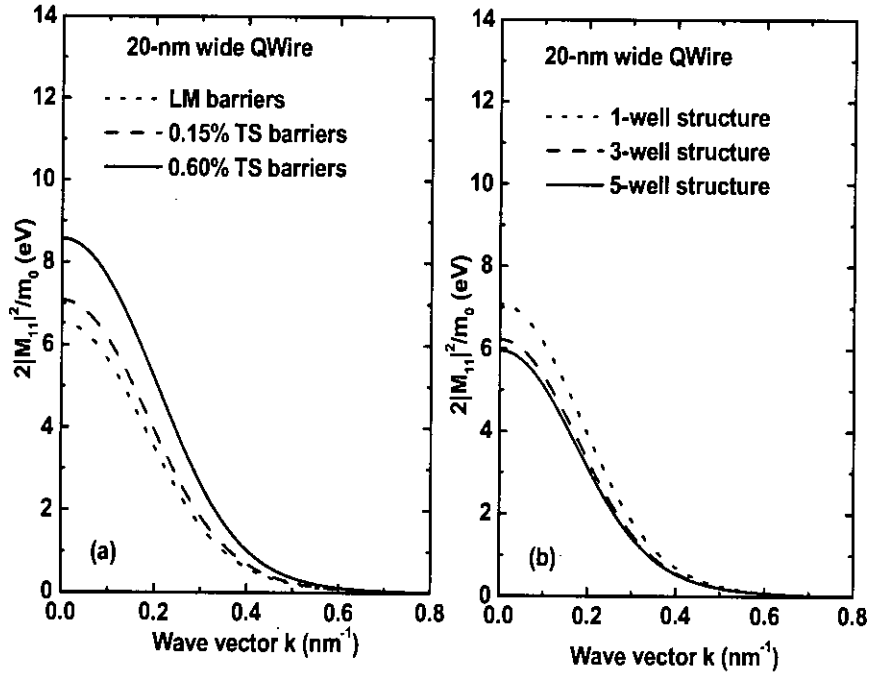


Figure 4.3: Transition matrix elements M_{11} as functions of wave vector k in a 20-nm-wide QWire for three types of barriers (a) and for different number of QWire layers in the active region with 0.15% TS barriers (b). Only $TE_{||}$ polarization are considered.

Fig. 4.6 shows the peak material gain G as a function of the injected carrier density n for different wire widths. It is evident that the transparency carrier density is reduced with the increase of the wire width. As the wire width is increased, the active region of the wire becomes more well-like and hence the band edge density of states becomes lower which reduces the transparency carrier density. Moreover, at higher carrier densities, G and differential gain (G') is higher for the 10-nm wide QWire compared to other structures. As the wire width is increased, peak gain is decreased and gain saturation is increased. This can be described in the following manner. As the wire width is increased, the number of bound levels is increased and the separation of these levels are decreased. As a result, occupation of excited levels become significant. Since these carriers do not contribute to gain, peak gain is reduced. Moreover, at higher carrier densities, peak gain may switch from the fundamental transition to the first excited transition.

Fig. 4.7 shows G as a function of the injected carrier density in 10-nm, 20-

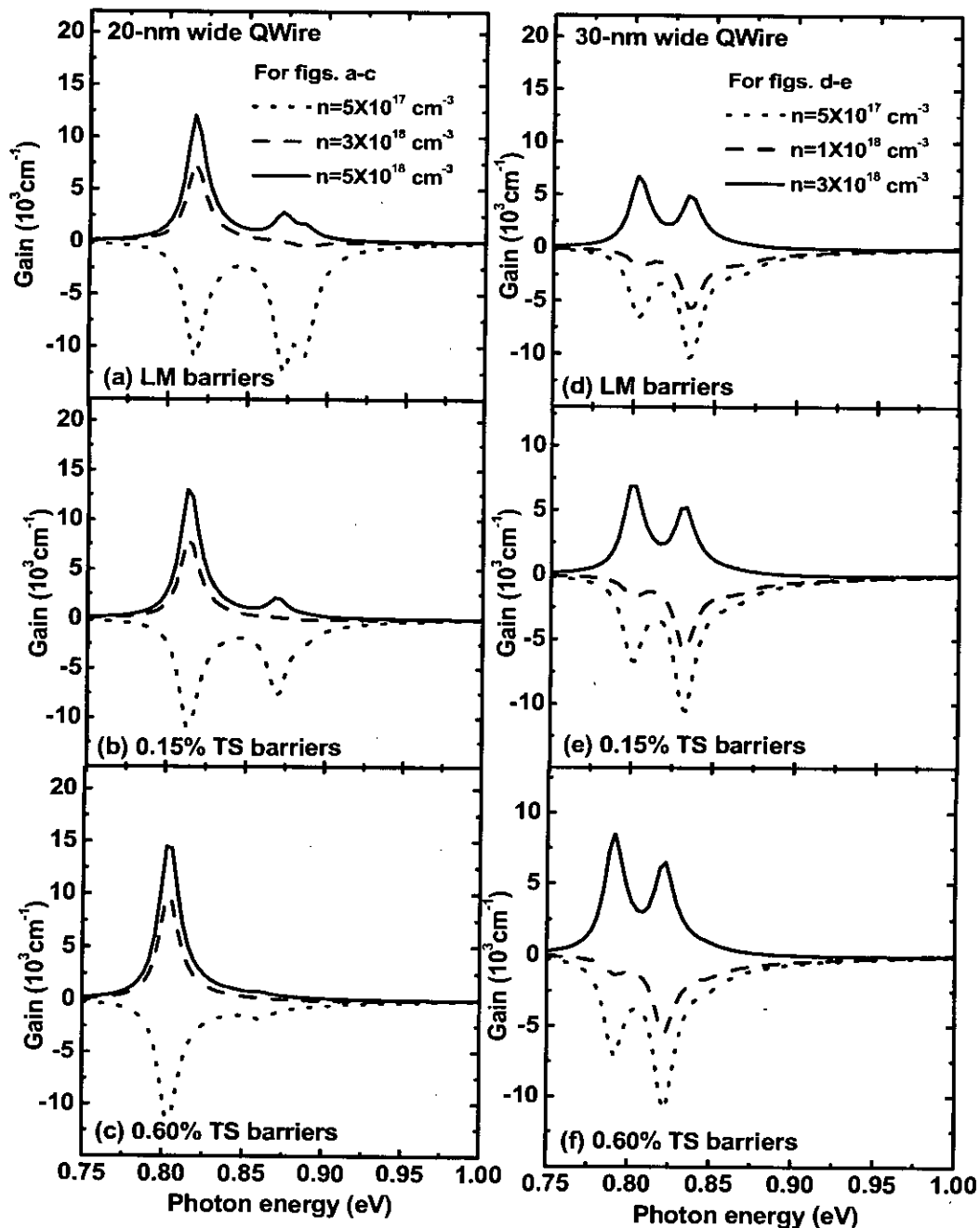


Figure 4.4: Material gain as a function of photon energy in a 20-nm-wide single-layer QWire (a-c), 30-nm-wide single-layer QWire (d-f) for LM and two types of TS barriers.

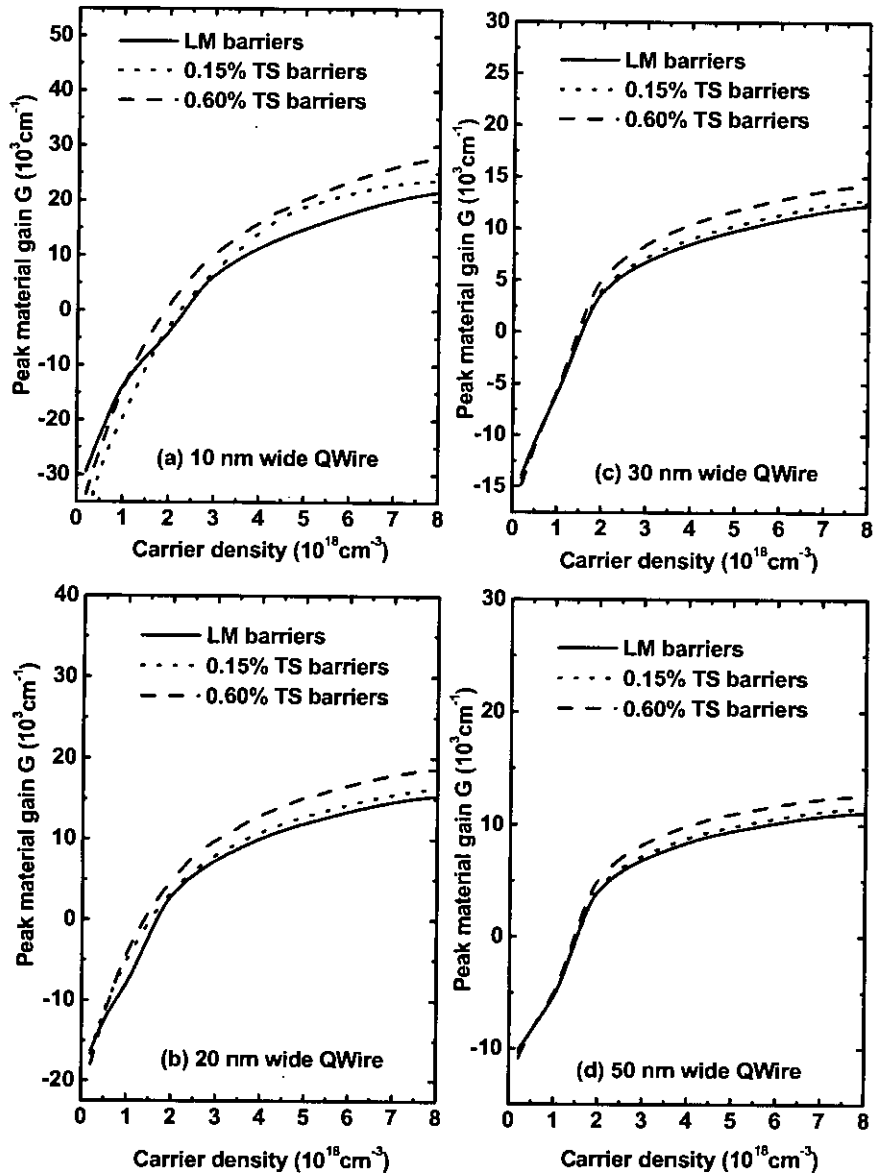


Figure 4.5: Peak material gain G at lasing frequency as a function of carrier density n in a 10-nm-wide QWire (a), 20-nm-wide QWire (b), 30-nm-wide QWire (c) and 50-nm-wide QWire (d) for LM and two TS barriers. QWires of single-layer structure are considered.

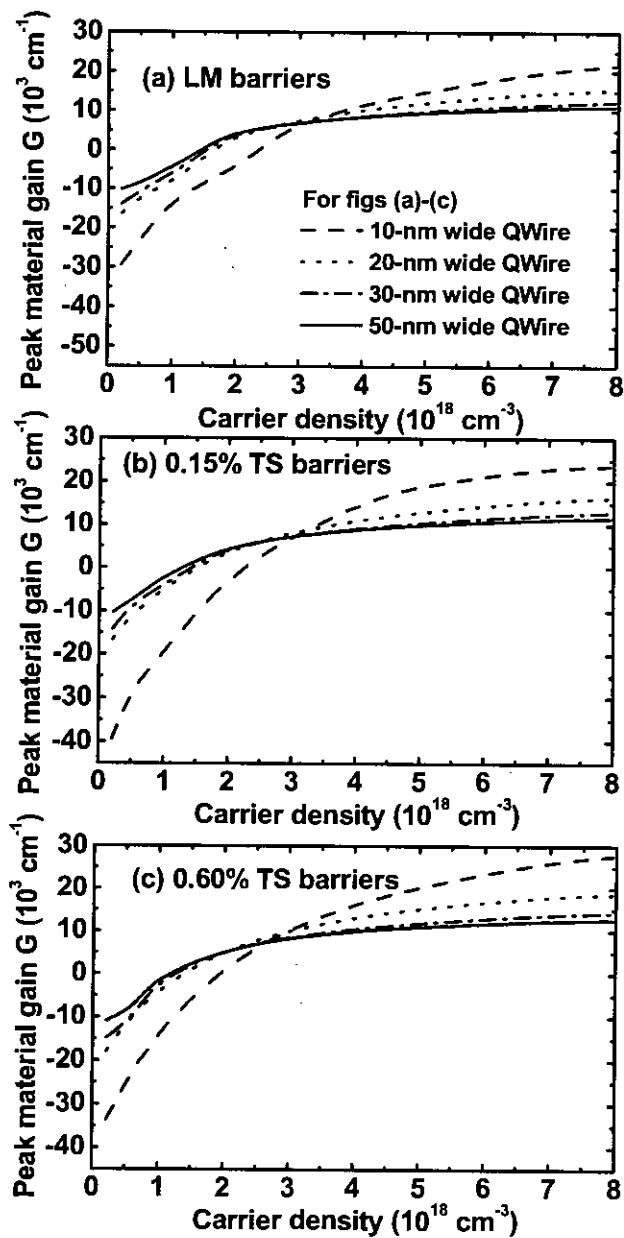


Figure 4.6: Peak material gain G as a function of carrier density n in a single-layer QWire structure with LM and two types of TS barriers for different wire widths (a)-(c).

nm and 50-nm QWires for different number of vertically stacked QWire layers in the active region of the QWire structures. It is observed that G is lower for the multi-layer QWires compared to its single-layer counterpart for all the wire widths. This is due to the relatively lower transition strengths of M_{11} as described in Fig. 4.3(b). However, the modal gain for the multi-layer QWires is larger compared to the single-layer QWires. Again, multi-layer QWires exhibit higher transparency carrier density for all the wire widths. This is due to the lower values of the peak gain.

4.3 Refractive Index Change

Fig. 4.8 presents carrier induced refractive index changes in 10-nm and 20-nm wide QWires. The procedures for calculating these quantities are described in Section 3.8. Both the real and imaginary refractive index changes for LM and two types of TS barriers are shown in the figure. It is clear that QWires with highly TS barriers show the lowest changes in both the real and imaginary part of the refractive indices as functions of carrier density. The opposite is true for QWires with LM barriers. Moreover, before the threshold carrier density is reached, QWires with LM barriers show a peak followed by a dip in the imaginary refractive index of both the structures. This is a direct consequence of the ripple present in the peak gain vs carrier density curves (Figs. 4.5 and 4.6) for LM barriers. The waveguide loss used to calculate the threshold gain is given in Table 4.2 with $\alpha_{ac}=100 \text{ cm}^{-1}$, $\alpha_{pass}=5 \text{ cm}^{-1}$ and the period of the wires is 100 nm. The mirror reflectivity loss was taken into account assuming $r_1 = r_2 = 0.3$ and cavity length of 1000 μm . The values are taken from [48]. Here,

4.4 Linewidth Enhancement Factor

α -factor relates the changes in the real and imaginary parts of the refractive index due to the changes in the injected carrier density. In lasers, the linewidth is enhanced by this factor.

Fig. 4.9 presents α -factor as a function of the photon energy for different carrier densities for 20-nm and 50-nm wide QWires with 0.15% TS barriers. The

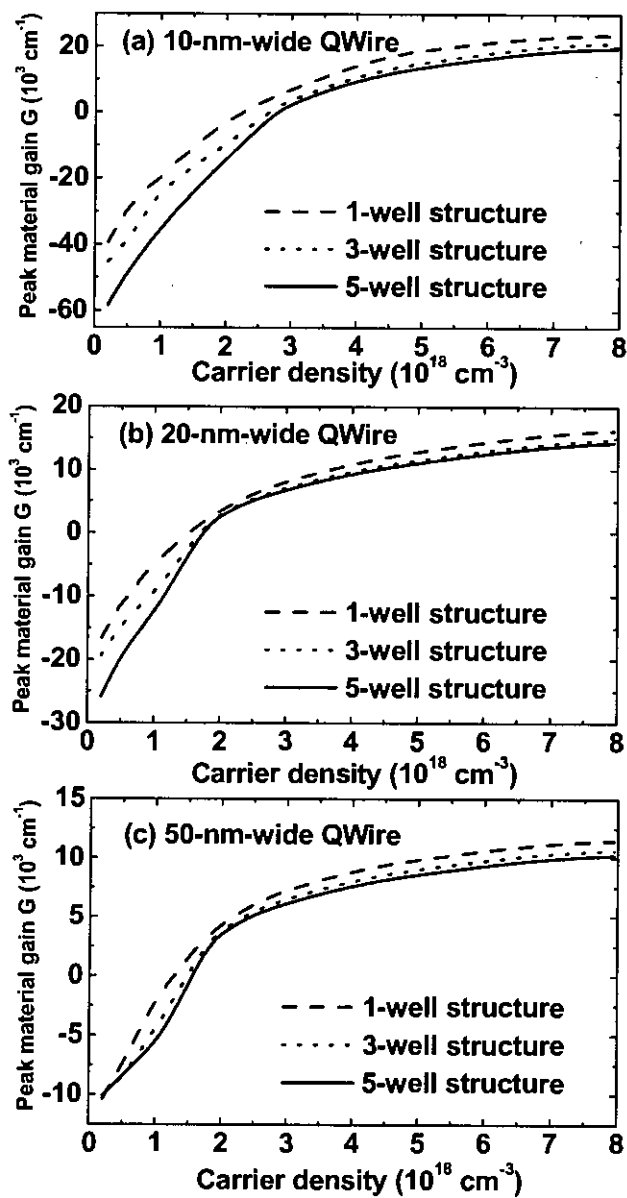


Figure 4.7: Peak material gain G as a function of carrier density n in 10-nm (a), 20-nm (b) and 50-nm (c) wide QWires with 0.15% TS barriers for different number of QWire layers in the active region.

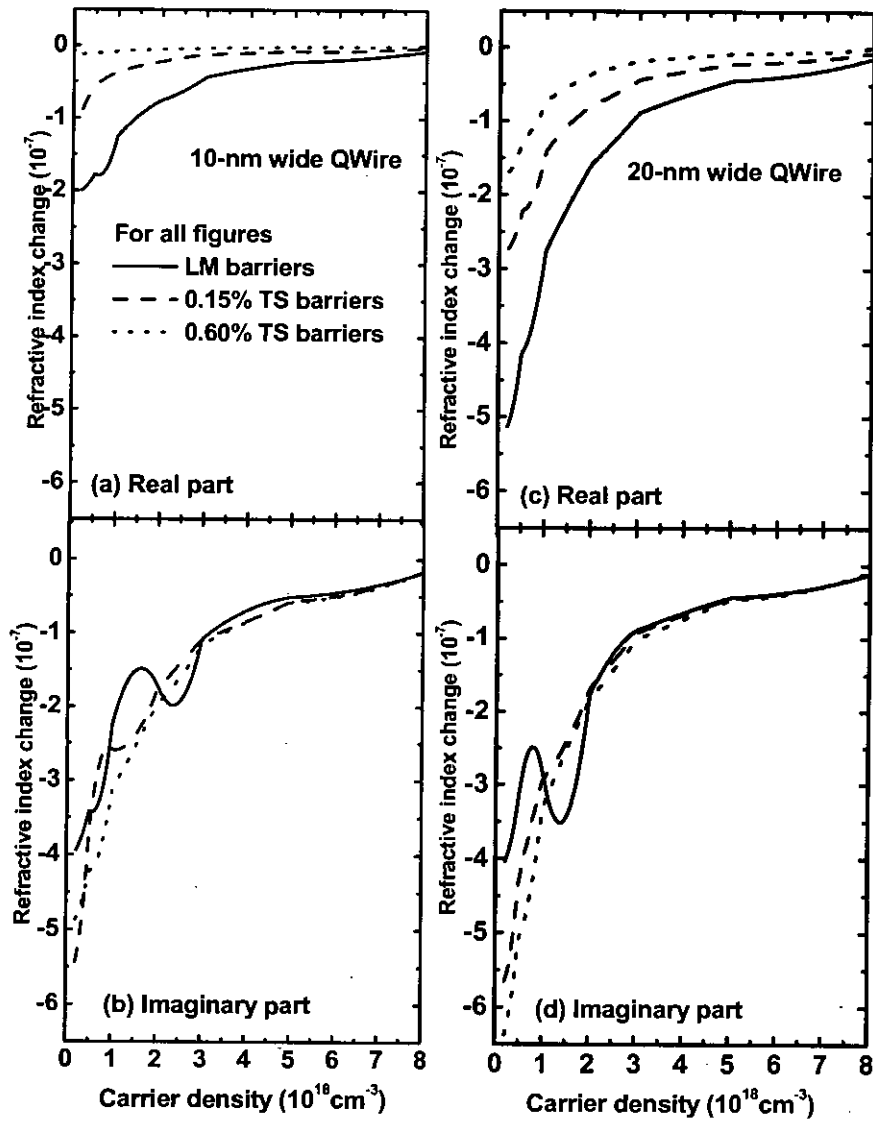


Figure 4.8: Both real part (a)-(b) and imaginary part (c)-(d) of refractive index change as a function of the injected carrier density at gain peak energy of single-layer QWire structures for wire widths of 10-nm and 20-nm, respectively.

arrows in the figures show the energy position where lasing would occur for the structures. The 20-nm wide QWire exhibits lower α -factor compared to the 50-nm wide QWire, as is expected. Moreover, the α -factor is more weakly dependent on the carrier densities in narrower QWires.

4.4.1 Variation of Barrier Strain

Fig. 4.10 presents α -factor at lasing frequencies as a function of the injected carrier density for different QWire structures with various barrier conditions. It is found that α -factor is the highest when the barriers are LM to the InP substrate and is drastically reduced when the TS in the barriers is increased in an SC scheme for all the structures. It is known that elastic strain relaxation in QWires depends on the barrier strain. SC barriers significantly reduce strain relaxation. Peak gain in TE mode for our cavity configuration is found to decrease with increasing strain relaxation (Fig. 4.5). Therefore, by using TS barriers, peak gain and differential gain are improved (Fig.4.5), which consequently reduces α -factor. Moreover, with LM barriers, for a particular QWire structure, say, for example 10-nm wide QWire (Fig. 4.10(a)), α -factor shows strong carrier density dependence until transparency carrier density is achieved. This is due to the manner the changes in the imaginary part of the refractive index expresses with increasing carrier densities before the transparency level is reached as is evident from Fig. 4.8(b). The same explanation holds for other structures. QWire structures with wider wire width shows larger values of α -factor compared to QWires with narrower wire width, also evident from Fig. 4.10.

4.4.2 Variation of number of QWire layers in the active region

Fig. 4.11 presents α -factor as a function of the injected carrier density in different QWire structures with 0.15% TS barriers for various number of QWells in the active region. It is found that α -factor is larger in case of single-layer QWires for all the structures and subsequently is reduced with the introduction of the multi-layer stacks in active region of the QWires. Modal gain in case of the QWires with 5-layer structures is about 5-times larger than the single-layer structures, which increases the changes in the imaginary part of the refractive index, thereby

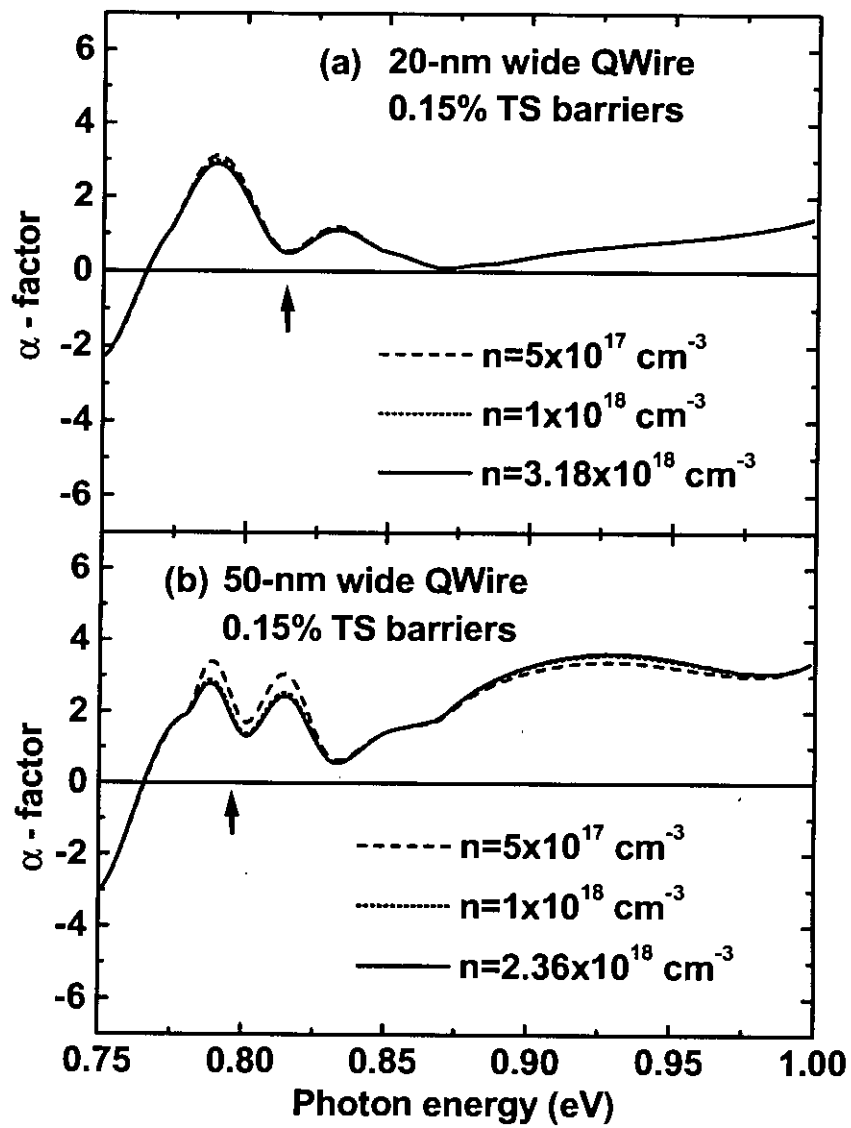


Figure 4.9: α -factor as a function of photon energy for single-layer QWire structure with wire widths of 20-nm (a), and 50-nm (b). The arrows point at the photon energy at which lasing would occur.

Table 4.2: Wave guide loss of single-layer QWires and QWell for 0.15% TS barriers with mode occupation factor, Γ_{act} of 1%/well.

Wire width (nm)	Waveguide loss (cm^{-1})
10	5.095
20	5.190
30	5.285
50	5.475
QWell	5.950

reducing the α -factor. However, as the number of quantum wells in the active region is increased, threshold carrier density is increased as is evident from Fig. 4.7.

4.4.3 Variation of Wire width

Fig. 4.12 presents the α -factor as a function of the injected carrier density in QWire structures for different barrier strain with increasing wire width. It is found that α -factor decreases significantly with decreasing wire width and exhibits less dependence on carrier density. This is due to the fact that peak gain increases and gain saturation decreases with decreasing wire width as is shown in Fig. 4.6. It is clear that 10-nm wide QWire exhibits the lowest α -factor for all the barrier conditions and it is increased with increasing wire width. Moreover, QWires with TS barriers shows further reduction in the α -factor, for peak gain is increased significantly in case of TS barriers in SC scheme.

Fig. 4.13(a) presents the material gain spectra as a function of the photon energy while Fig. 4.13(b) presents the peak material gain as a function of the injected carrier density in a QWell laser, both for 0.15% TS barriers. It is to be noted from the figures that QWell lasers exhibit lower material gain for a particular carrier density compared to the QWire lasers as presented in Figs. 4.4 and 4.6, respectively. This is due to the increased dimensionality in the QWell lasers compared to the QWire lasers. It is also noted from Fig. 4.13(a) that the gain broadening in QWell structure is more than the QWires, also clear from Fig. 4.4. Table 4.3 presents the lasing wavelength, threshold carrier density and α -factor at threshold carrier density for different wire widths and also for QWell structure with 0.15% TS barriers and with single-layer stack.

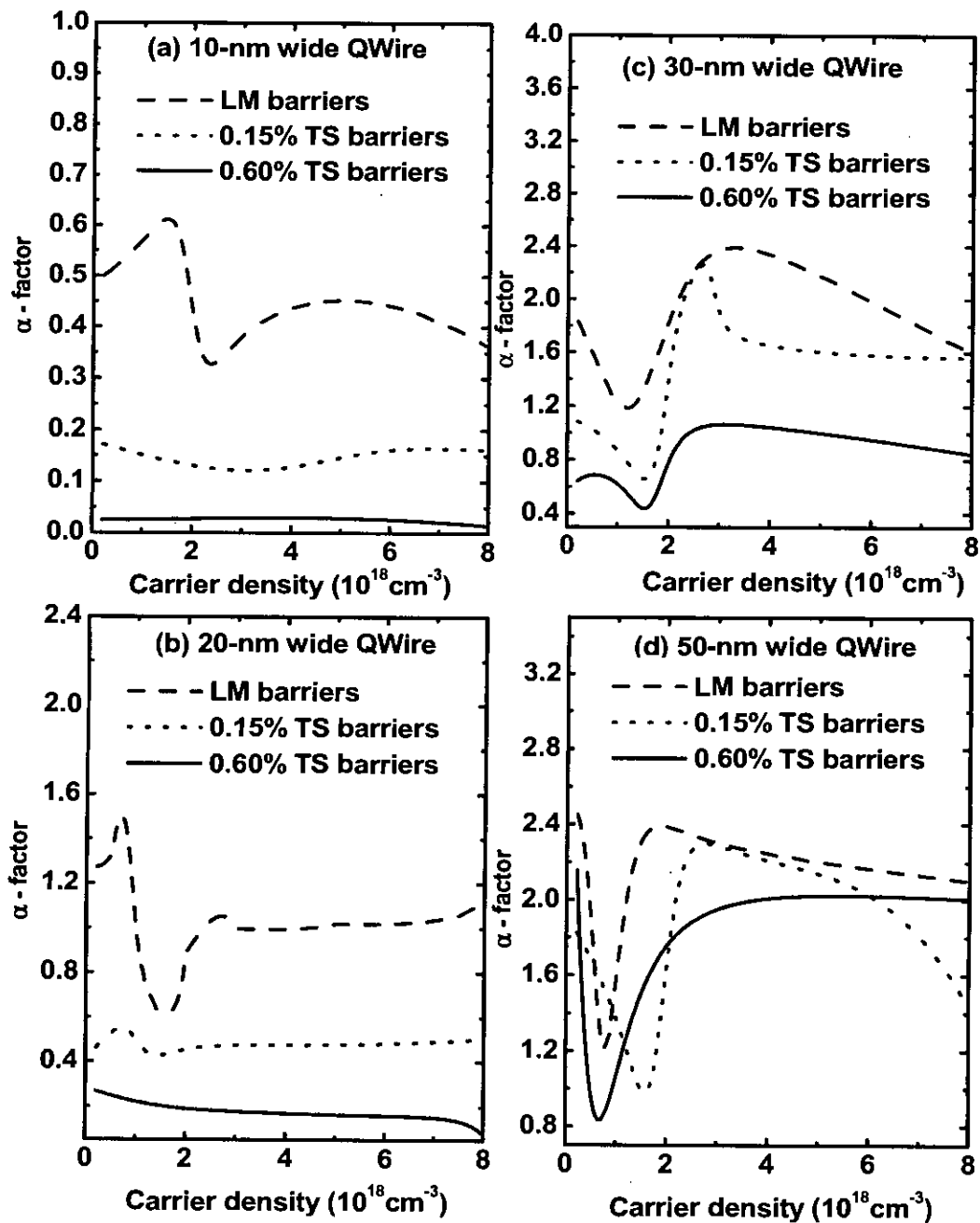


Figure 4.10: α -factor as a function of the injected carrier density at gain peak position of single-layer QWire structure with LM and two types of TS barriers for wire widths of (a) 10-nm, (b) 20-nm, (c) 30-nm and (d) 50-nm.

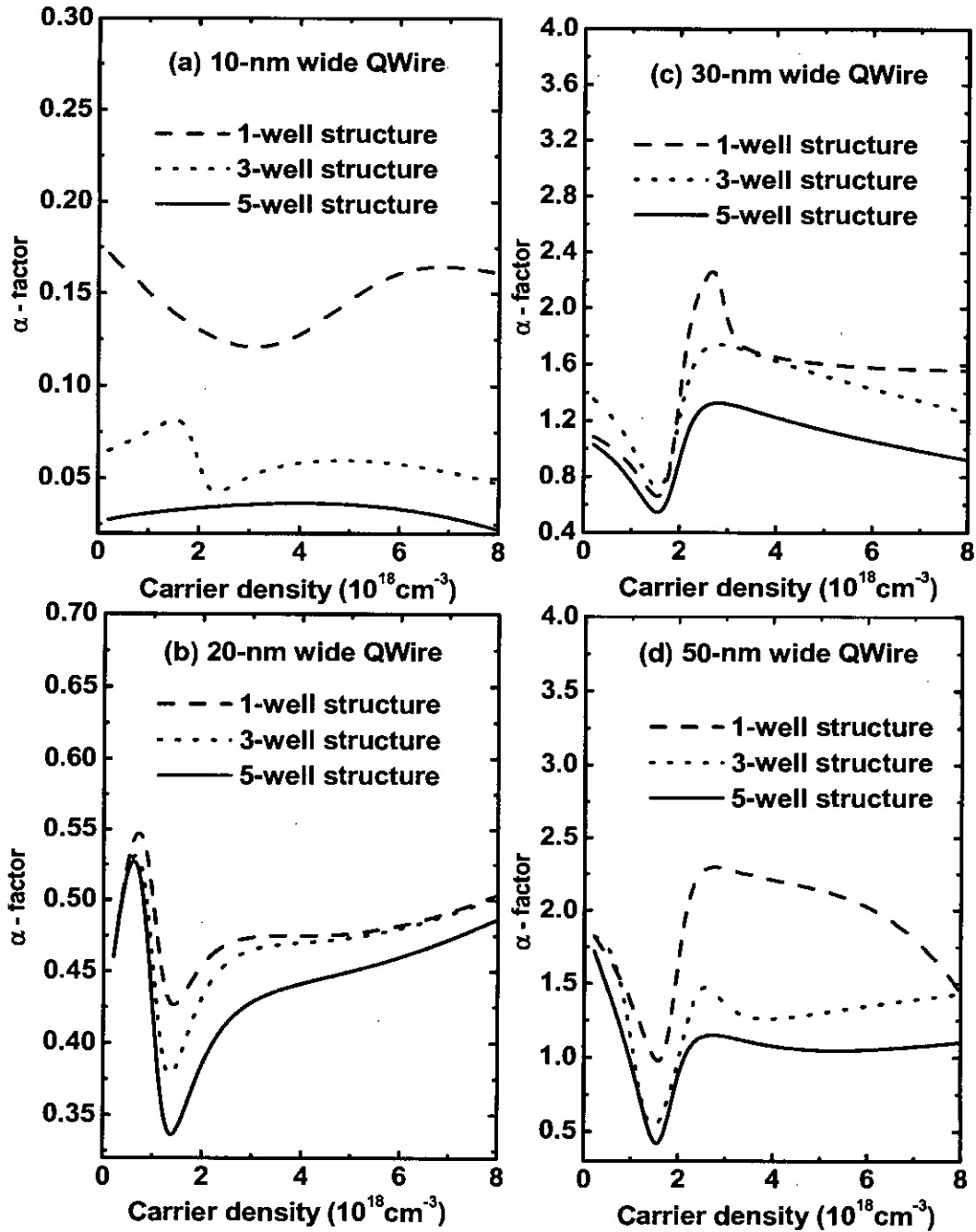


Figure 4.11: α -factor as a function of the injected carrier density at gain peak position of QWire structures with different number of QWire layers with 0.15% TS barriers for wire widths of (a) 10-nm, (b) 20-nm, (c) 30-nm and (d) 50-nm.

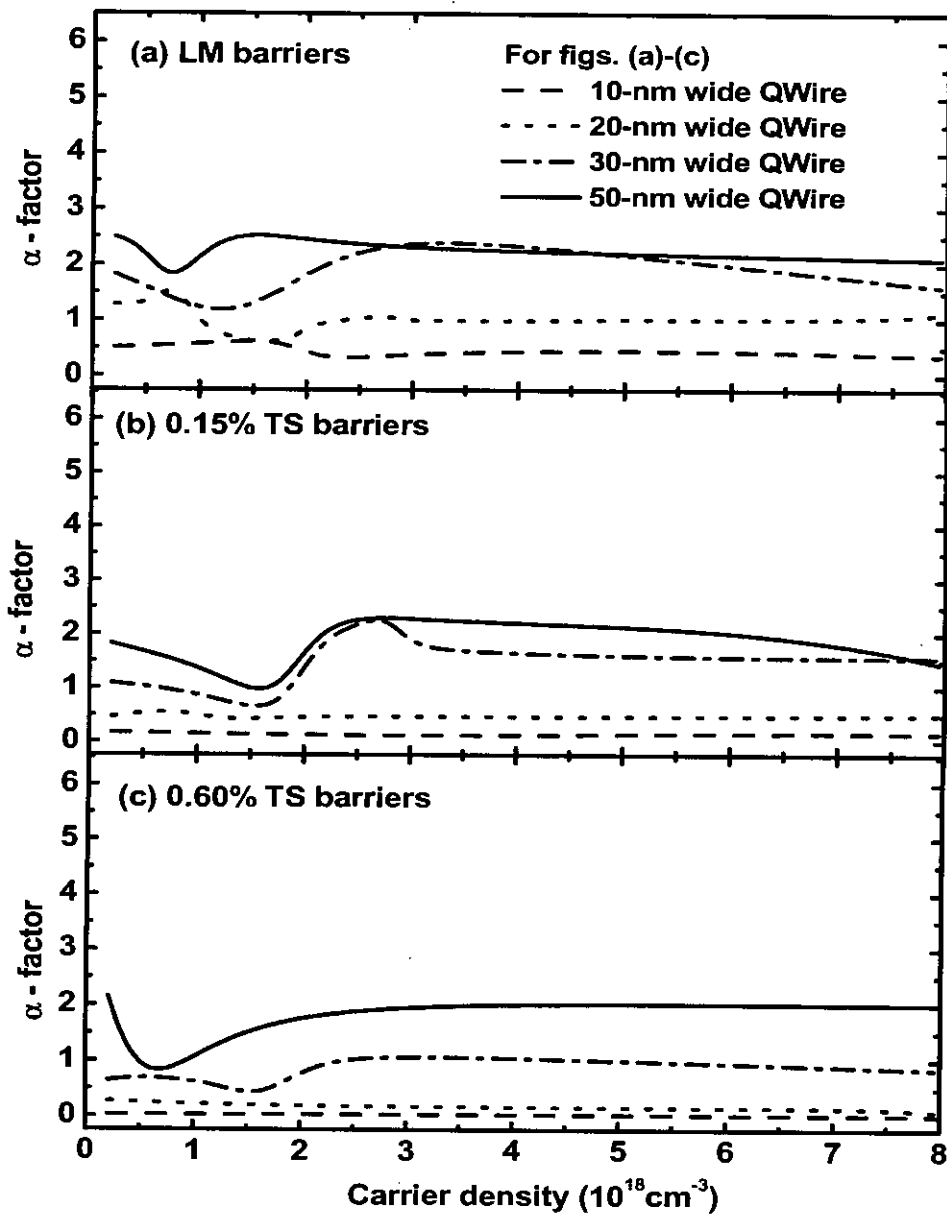


Figure 4.12: α -factor as a function of the injected carrier density at gain peak position of single-layer QWire structures with different wire widths for (a) LM (b) 0.15% TS and (c) 0.60% TS barriers.

Table 4.3: Lasing wavelength, threshold carrier density and α -factor for different QWires and QWell structure with 0.15% TS barriers and with single-layer stack.

Wire width (nm)	Lasing wavelength (μm)	Threshold carrier density (10^{18} cm^{-3})	α -factor at threshold
10	1.46	4.61	0.13866
20	1.52	3.18	0.47432
30	1.54	2.81	2.1795
50	1.56	2.36	2.2022
QWell	1.58	2.67	1.0603

Finally, α -factor for a QWell structure is presented in Fig. 4.14 in order to make the comparison with that of the QWire structures, for LM and two types of TS barriers. All the α -factors are evaluated at the respective lasing frequencies, or at the gain peak frequencies. Among all the structures with both LM and TS barriers, the maximum value of the α -factor is the highest for the QWell, and this maxima monotonically decreases with decreasing wire width. This observation is in agreement with the theoretical predictions, as is clear from Table 4.3. Lasing wavelength increases with increasing wire widths and the QWell structure shows the maximum value, as expected. With the increase of the wire width, threshold carrier densities are decreased. The reason behind this has already been discussed. However, the QWell structure shows a significant value of the threshold carrier density for the same loss condition. This is because the peak gain of the QWell structure is much less than the QWires. α -factor at threshold increases with the increase of the wire widths, as expected. It is found for the structure with 0.15% TS barriers that in spite of the reduction of the maximum value of the α -factor with decreasing wire width, improvement relative to QWell lasers is not achieved for the threshold α -factor unless the wire width is reduced below 30 nm.

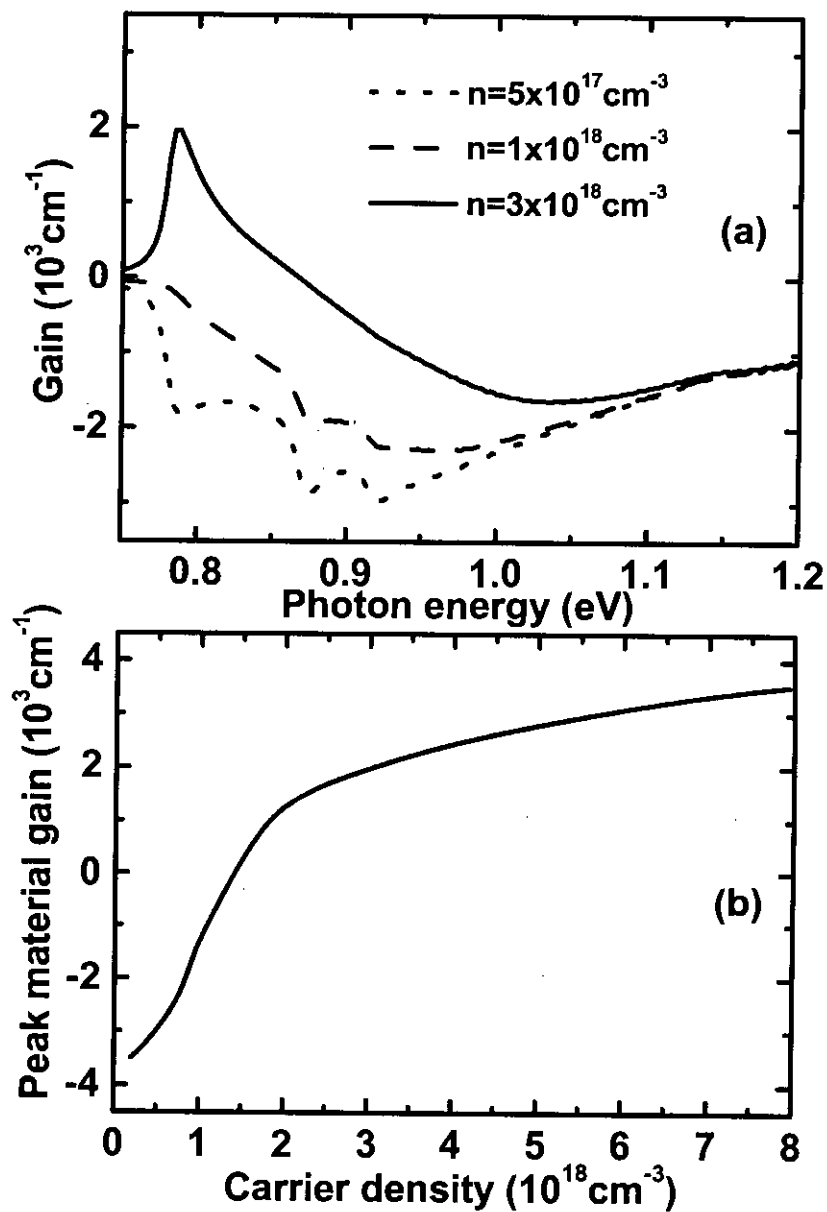


Figure 4.13: Material gain as a function of the photon energy (a) and peak material gain as a function of the injected carrier density (b) for a QWell laser with 0.15% TS barriers.

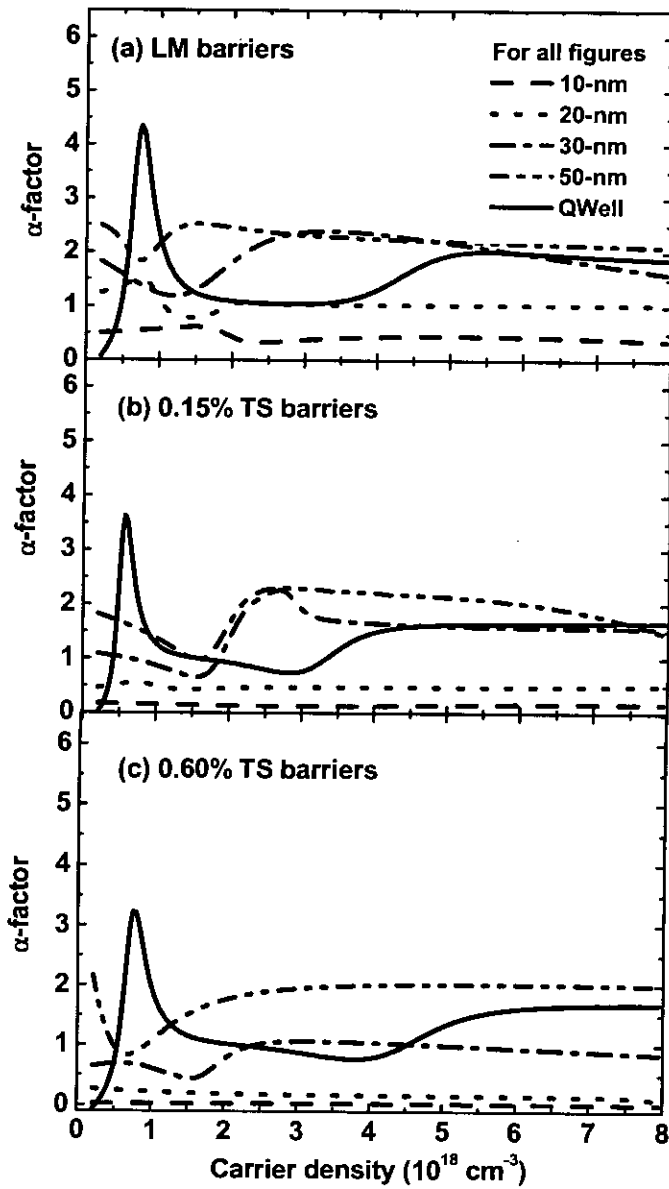


Figure 4.14: α -factor as a function of the injected carrier density for different wire widths with LM and two types of TS barriers. α -factor for QWell structure is also presented for comparison.

Chapter 5

Conclusions

A numerical method to analyze the dynamic performances of QWire lasers has been studied. Results show that α -factor depends on the device parameters, such as, wire width, barrier strain, number of vertical layers etc., in a complicated way owing to the complex interactions between 2D quantum confinement and elastic strain relaxation effects. Therefore, to optimize the device structures for reduced α -factor, it is necessary to investigate in detail the dependence of α -factor on these parameters including non-parabolicity, elastic strain relaxation and other important effects.

5.1 Summary

α -factor, which describes the carrier induced coupling of the gain change to the refractive index change in the active region, is one of the most important parameters to characterize the dynamic performance of semiconductor lasers. Improved performance of semiconductor lasers can be obtained by incorporating low-dimensional structures in the active regions. The QWire structure under the consideration of this work consists of multiple layers of InGaAsP CS QWires and TS or LM barriers grown on (001) InP substrate. Effects of non-parabolicity due to material properties, quantum-confinement and elastic strain relaxation are incorporated in the calculations. The band structures of the CS InGaAsP QWires are first calculated using an 8 band $\mathbf{k} \cdot \mathbf{p}$ model including elastic strain relaxation effects. Optical transitions between electronic states are evaluated using Fermi's golden rule. Changes in imaginary part of the refractive index is easily found from the gain spectra and changes in real part of the refractive index is evaluated

from the changes in imaginary part through Kramers-Kronig transformation. All the calculations are for TE gain which is dominant in CS structures. For QWires, the electric field of the radiation is assumed to be along the wire axis and the laser cavity is considered to be perpendicular to the wire axis. Dependence of α -factor, which enhances the linewidth of a laser, on device parameters such as wire width, barrier strain and number of vertically stacked QWire layers, are evaluated and fundamental trend in the behavior of the α -factor is investigated. It is found that α -factor decreases significantly with decreasing wire width and exhibits less dependence on carrier density. Also, α -factor is the highest when the barriers are LM to the InP substrate and is drastically reduced when the TS in the barriers is increased in a strain compensating (SC) scheme. It is known that elastic strain relaxation in QWires depends on the barrier strain. SC barriers strongly suppress strain relaxation. Peak gain in TE mode for the cavity configuration is found to increase with suppressing strain relaxation. Therefore, by using TS barriers, peak gain and differential gain are improved, which consequently reduces α -factor. Moreover, QWire structures with multiple-layer exhibits lower value of α -factor compared to the one with single-layer structure. This is because modal gain in case of multiple-layer structure is greater than the single-layer structure due to its higher mode occupation factor. Finally, α -factor for a QWell laser is calculated and compared to the QWires in order to identify the improvements due to the reduced dimensionality in the QWires. It is found that improvements in the α -factor relating to QWell laser is not achieved unless wire width is reduced below 30 nm. However, among all the structures, the maximum value of the α -factor is the highest for the QWell and this maxima monotonically decreases with decreasing wire width.

5.2 Suggestions for Future Works

Semiconductor lasers are key devices in order to realize ultra-fast communications using optical fibres. The dynamic performances of QWire laser structures are analyzed by varying its various device parameters, such as, wire width, barrier strain, number of quantum well layers in the active region. The barrier strain has been analyzed assuming isotropic strain relaxation. For more accuracy, anisotropic strain relaxation can be analyzed. α -factor has been determined for each de-

at their individual lasing frequencies, which ranges from $1.46 \mu\text{m}$ - $1.56 \mu\text{m}$. However, the device structures can be modified so that each device lases at $1.55 \mu\text{m}$, the wavelength of the most interest. This will make the comparison of the α -factor more meaningful. In this analysis, only the first order relationship between the carrier density and the real and the imaginary parts of the refractive index has been considered. Higher order relationships should lead to new effects and might modify the α -factor. Therefore, further work is necessary to calculate α -factor including higher order effects. Finally, QWires only with rectangular cross-sections fabricated by EBL and two step MOCVD growth have been considered in this work. The model may be extended to consider other types of QWire structures as well, such as crescent shaped V-groove QWires on GaAs substrate.

Bibliography

- [1] N. Holonyak, Jr., R. M. Kolbas, R. D. Dupuis, and P. D. Dapkus, "Quantum-well heterostructure lasers," *IEEE J. Quantum Electron.*, vol. QE-16, no. 2, pp. 170-186, Feb. 1980.
- [2] Y. Arakawa, and H. Sakaki, "Multidimensional quantum well laser and temperature dependence of its threshold current," *Appl. Phys. Lett.*, vol. 40, no. 11, pp. 939-941, June 1982.
- [3] M. Asada, Y. Miyamoto, and Y. Suematsu, "Gain and threshold of three-dimensional quantum-box lasers," *IEEE J. Quantum Electron.*, vol. QE-22, no. 9, pp. 1915-1921, Sep. 1986.
- [4] E. Yablonoitch, and E. Kane, "Reduction of lasing threshold current density by the lowering of valence band effective mass," *IEEE J. Lightwave Technol.*, vol. 4, no. 5, pp. 516-519, 1986.
- [5] A. R. Adams, "Band structure engineering for low- threshold high-efficiency semiconductor lasers," *Electron. Lett.*, vol. 22, pp. 249-250, 1986.
- [6] D. Nichols, M. Sherwin, G. Munns, J. Pamulapati, J. Loehr, J. Singh, P. Bhattacharya, and M. Ludowise, "Theoretical and experimental studies of the effects of compressive and tensile strain on the performance of InP-InGaAs multiquantum-well lasers," *IEEE J. Quantum Electron.*, vol. QE-28, no. 5, pp. 1239-1242, May 1992.
- [7] S. Colak, R. Eppenga, and M. F. H. Schuurmans, "Band mixing effects on quantum-well gain," *IEEE J. Quantum Electron.*, vol. QE-23, no. 6, pp. 960-968, June 1987.

- [8] G. Jones, and P. O'Reilly, "Improved performance of long wavelength strained bulk-like semiconductor lasers," *IEEE J. Quantum Electron.*, vol. 29, no. 5, pp. 1344-1354, May 1993.
- [9] A. Mozer, K. M. Romanek, O. Hidrebrand, W. Schmid, and M. H. Pilkuhn, "Losses in GaInAs(P)/InP and GaAlSb(As)/GaSb lasers- the influence of the split-off valence band," *IEEE J. Quantum Electron.*, vol. QE-19, no. 6, pp. 913-916, June 1983.
- [10] J. P. Loehr, and J. Singh, "Theoretical studies of the effect of strain on the performance of strained quantum well lasers based on GaAs and InP technology," *IEEE J. Quantum Electron.*, vol. 27, no. 3, pp. 708-716, March 1991.
- [11] G. E. Pikus, and G. L. Bir, "Effects of deformation on the hole energy spectrum of germanium and silicon," *Sov. Phys. Solid State*, vol. pp. 1502-1517, 1960.
- [12] K. Nishi, A. A. Yamaguchi, J. Ahopelto, A. Usui, and H. Sakaki, "Analysis of localized confinement potential in semiconductor strained wires and dots buried in lattice-mismatched materials," *J. Appl. Phys.*, vol. 76, no. 11, pp. 7437-7445, Dec. 1994.
- [13] D. Ahn, and S. L. Chuang, "Optical gain and gain suppression of quantum-well lasers with valence band mixing," *IEEE J. Quantum Electron.*, vol. 26, no. 1, pp. 13-25, Jan. 1990.
- [14] Y. Arakawa, and A. Yariv, "Quantum well lasers-gain, spectra, and dynamics," *IEEE J. Quantum Electron.*, vol. QE-22, no. 9, pp. 1887-1899, Sep. 1986.
- [15] D. Ahn, and S. L. Chuang, "Optical gain in a strained-layer quantum-well laser," *IEEE J. Quantum Electron.*, vol. 24, no. 12, pp. 2400-2406, Dec. 1988.
- [16] T. A. Ma, Z. M. Li, T. Makino, and M. S. Wartak, "Approximate optical gain formula for 1.55- μm strained quaternary quantum-well lasers," *IEEE J. Quantum Electron.*, vol. 31, no. 1, pp. 29-34, Jan. 1995.

- [17] J. S. Osinski, P. Grodzinski, Y. Zou, and P. D. Dapkus, "Threshold current analysis of compressive strain (0-1.8%) in low-threshold, long-wavelength quantum well lasers," *IEEE J. Quantum Electron.*, vol. 29, pp. 1576-1585, June 1993.
- [18] N. Yokouchi, N. Yamaraka, N. Iwai, and A. Kasukawa, " $Ga_xIn_{1-x}As_yP_{1-y}$ -*InP* tensile-strained quantum wells for 1.3- μ m low-threshold lasers," *IEEE J. Quantum Electron.*, vol. 29, pp. 1576-1585, June 1993.
- [19] G. Jones, A. D. Smith, E. P. O'Reilly, M. Silver, A. T. R. Briggs, M. J. Fice, A. R. Adams, P. D. Greene, K. Scarrot, and A. Vranic, "The influence of tensile strain on differential gain and Auger recombination in 1.5- μ m multiple-quantum-well lasers," *IEEE J. Quantum Electron.*, vol. 34, pp. 822-833, May 1998.
- [20] J. Downes, and D. A. Faux, "Calculation of strain distributions in multiple-quantum-well strained-layer structures," *J. Appl. Phys.*, vol. 77, no. 6, pp. 2444-2447, March 1995.
- [21] J. Downes, D. A. Faux, and E. P. O'Reilly, "Influence of strain relaxation on the electronic properties of buried quantum wells and wires," *Mat. Science and Engg.*, vol. B35, pp. 357-363, 1995.
- [22] D. A. Faux, S. G. Howells, U. Bangert, and A. J. Henry, "Strain relaxation in strained buried heterostructure lasers," *Appl. Phys. Lett.*, vol. 64, no. 10, pp. 1271-1273, March 1994.
- [23] H. Yagi, T. Sano, K. Ohira, T. Maruyama, A. Haque, and S. Arai, "Room temperature-continuous wave operation of GaInAsP/*InP* multiple-quantum-wire lasers by dry etching and regrowth method," *Jpn. J. Appl. Phys.*, pt. 2, vol. 42, no. 7A, pp. 48-50, July 2003.
- [24] M. Yamada, and Y. Haraguchi, "Linewidth broadening of SCH quantum-well lasers enhanced by carrier fluctuation in optical guiding layers," *IEEE J. Quantum Electron.*, vol. 27, no. 6, pp. 1676-1681, June 1991.
- [25] C. H. Henry, "Theory of the linewidth of semiconductor lasers," *IEEE J. Quantum Electron.*, vol. QE-18, no. 2, pp. 259-264, Feb. 1982.

- [26] M. Fujise, "Spectral linewidth estimation of a 1.5- μm range InGaAsP/InP distributed feedback laser," *IEEE J. Quantum Electron.*, vol. QE-22, no. 3, pp. 458-462, March 1986.
- [27] J. P. Van Der Ziel, "Spectral broadening of pulsating $\text{Al}_x\text{Ga}_{1-x}\text{As}$ double heterostructure lasers," *IEEE J. Quantum Electron.*, vol. QE-15, no. 11, pp. 1277-1281, Nov. 1979.
- [28] F. R. Nash, "Mode guidance parallel to the junction plane of double heterostructure GaAs lasers," *J. Appl. Phys.*, vol. 44, pp. 4696-4706, Oct. 1973.
- [29] G. H. B. Thompson, "A theory for filamentation in semiconductor lasers including the dependence of dielectric constant on injected carrier density," *Opto. Electron.*, vol. 4, pp. 257-310, Aug. 1972.
- [30] M. Cross, and M. J. Adams, "Effects of doping and free carriers in the refractive index of direct gap semiconductors," *Opto. Electron.*, vol. 6, pp. 199-216, 1974.
- [31] M. Ito, and T. Kimura, "Carrier density dependence of refractive index in AlGaAs semiconductor lasers," *IEEE J. Quantum Electron.*, vol. QE-16, no. 9, pp. 910-911, Sep. 1980.
- [32] C. H. Henry, R. A. Logan, and K. A. Bertness, "Spectral dependence of the change in refractive index due to carrier injection in GaAs lasers," *J. Appl. Phys.*, vol. 52, no. 7, pp. 4457-4461, July 1981.
- [33] Y. Arakawa, and A. Yariv, "Theory of gain, modulation response and spectral linewidth in AlGaAs quantum well lasers," *IEEE J. Quantum Electron.*, vol. QE-21, no. 10, pp. 1666-1674, Oct. 1985.
- [34] M. Osiński, and J. Buus, "Linewidth broadening factor in semiconductor lasers- an overview," *IEEE J. Quantum Electron.*, vol. QE-23, no. 1, pp. 9-26, Jan. 1987.
- [35] M. P. Mullane, and J. G. McInerney, "Minimization of the linewidth enhancement factor in tensile-strained quantum-well lasers," *IEEE Photon Technol. Lett.*, vol. 12, no. 9, pp. 1147-1149, Sep. 2000.

- [36] M. Willatzen, T. Tanaka, Y. Arakawa, and J. Singh, "Polarization dependence of optoelectronic properties in quantum dots and quantum wires- consequences of valence band mixing," *IEEE J. Quantum Electron.*, vol. 30, no. 3, March 1994.
- [37] W. H. Seo, and B. H. Han, "Many body effects on the linewidth enhancement factor of strained quantum wire lasers," *Solid State Communications*, vol. 119, pp. 367-369, 2001.
- [38] W. H. Seo, and B. H. Han, "Spin-orbit coupling effects on the linewidth enhancement factor of strained quantum wire lasers," *Solid State Communications*, vol. 115, pp. 297-300, 2000.
- [39] J. Oksanen, and J. Tulkki, "Linewidth enhancement factor and chirp in quantum dot lasers," *J. Appl. Phys.*, vol. 94, no. 3, pp. 1983-1989, Aug. 2003.
- [40] S. Schneider, P. Borri, W. Langbein, U. Woggon, R. L. Sellin, D. Ouyang, and D. Bimberg, "Linewidth enhancement factor in InGaAs quantum-dot amplifiers," *IEEE J. Quantum Electron.*, vol. 40, no. 10, pp. 1423-1429, Oct. 2004.
- [41] M. W. Fleming, and A. Mooradian, "Fundamental line broadening of single mode (GaAl)As diode lasers," *Appl. Phys. Lett.*, vol. 38, pp. 511, 1981.
- [42] J. M. Luttinger, and W. Kohn, "Motion of electrons and holes in perturbed periodic fields," *Phys. Rev.* vol. 97, no. 4, pp. 869-876, Feb. 1955.
- [43] P. C. Sercel, and K. J. Vahalla, "Analytical formalism for determining quantum wire and quantum dot band structure in the multi-band envelope function approximation," *Phys. Rev.*, vol. B42, pp. 3690-3710, 1990.
- [44] D. Gershoni, C. H. Henry, and G. A. Baraff, "Calculating the optical properties of multidimensional heterostructures: application to the modeling of quaternary quantum well lasers," *IEEE J. Quantum Electron.*, vol. 29, no. 9, pp. 2433-2450, Sep. 1993.

- [45] S. W. Corzine, R. Yan, and L. A. Coldren, "Optical gain in III-V bulk and quantum well semiconductors," in *Quantum Well Lasers*. P. Zory, Ed. New York: Academic Press, pp. 28-32, 1993.
- [46] R. E. Nahory, M. A. Pollack, and W. D. Johnston, Jr., "Bandgap versus composition and demonstration of Vegard's law for $In_{1-x}Ga_xAs_yP_{1-y}$ lattice matched to InP ," *Appl. Phys. Lett.*, vol. 33, no. 7, pp. 659-661, Oct. 1978.
- [47] A. Haque, H. Yagi, T. Sano, T. Maruyama, and S. Arai, "Electronic band structures of GaInAsP/InP stacked multiple quantum wires with strain compensating barriers," *J. Appl. Phys.*, vol. 94, no. 3, pp. 2018-2023, 2003.
- [48] N. Nunoya, M. Nakamura, H. Yasumoto, S. Tamura, and S. Arai, "GaInAsP/InP multiple-layered quantum-wire lasers fabricated by CH_4/H_2 reactive-ion etching," *Jpn. J. Appl. Phys.*, pt. 1, vol. 39, no. 6A, pp. 3410-3415, June 2000.

